

A Novel Truncated Norm Regularization Method for Multi-channel Color Image Denoising

Yiwen Shan, Dong Hu, and Zhi Wang, *Member, IEEE*

Abstract—Due to the high flexibility and remarkable performance, low-rank approximation has been widely studied for color image denoising. However, existing methods usually ignore the cross-channel difference or the spatial variation of noise, which limits their capacity in the task of real world color image denoising. To overcome these drawbacks, this paper proposes a double-weighted truncated nuclear norm minus truncated Frobenius norm minimization (DtNFM) model, and apply it to color image denoising through exploiting the nonlocal self-similarity prior. The proposed DtNFM model has two merits. First, it models and utilizes both the cross-channel difference and the spatial variation of noise. This provides sufficient flexibility for handling the complex distribution of noise in real world images. Second, the proposed DtNFM model provides a close approximation to the underlying clean matrix since it can treat different rank components flexibly. To solve the DtNFM model, an efficient algorithm is devised through exploiting the framework of alternating directions method of multipliers (ADMM). Meanwhile, the truncated nuclear norm minus truncated Frobenius norm regularized least squares subproblem is discussed in detail, and the results show that its global optimum can be directly obtained in closed form. Therefore, the DtNFM model can be efficiently solved by a single ADMM. Rigorous mathematical derivation proves that the solution sequences generated by our proposed algorithm converge to a single critical point. Extensive experiments on synthetic and real noise datasets demonstrate that the proposed method outperforms many state-of-the-art color image denoising methods. MATLAB code is available at <https://github.com/wangzhi-swu/DtNFM>.

Index Terms—Color image denoising, Low-rank approximation, Truncated nuclear norm minus truncated Frobenius norm, ADMM

I. INTRODUCTION

IMAGE denoising serves as an indispensable process for manifold tasks in computer vision, such as semantic image segmentation [1], [2] and image retrieval [3], [4]. It aims to recover the clean image X from its corrupted observation Y , and such problem can be expressed as

$$Y = X + N, \quad (1)$$

where N is the white Gaussian noise. Since problem (1) is ill-posed, prior information should be exploited in order

to regularize the solution space and improve the denoising performance. With them, image denoising can be formulated as the following well-posed problem:

$$\arg \min_X \mathcal{F}(X) + \lambda \cdot \Phi(X), \quad (2)$$

where $\mathcal{F}(\cdot)$ is a loss function, $\Phi(\cdot)$ is a regularizer corresponding to some prior information, and λ is a parameter. In the past decade, a large amount of works have been carried out on image denoising. State-of-the-art methods are mainly based on sparse representation [5]–[8], deep learning [9]–[14], and low-rank approximation [15]–[21]. The sparse representation-based methods estimate the denoised images by finding a sparse linear combination of bases. And the bases can be learned from the observation. However, it is difficult for those methods to handle the spatially variant noise. The deep learning-based methods learn a function from a large amount of data. The function, in which the prior information are modeled implicitly, relates the corrupted image to the denoised results. However, their generalization are usually not good since the dependence on the training data.

Due to the high efficiency and strong denoising capability, low-rank approximation-based methods have been widely studied. Along this line, lots of state-of-the-art methods are proposed based on the nonlocal self-similarity (NSS) prior [22], [23]. NSS indicates that there spread many similar structures across a natural image. Those similar structures can be gathered to construct a corrupted patch matrix, denoted as \mathbf{Y} . Since the gathered patches have similar structures, matrix \mathbf{Y} is (or approximately) low rank. Hence its denoised version, denoted as \mathbf{X} , can be estimated by solving the following optimization problem:

$$\arg \min_{\mathbf{X}} \frac{1}{2\sigma_n^2} \|\mathbf{Y} - \mathbf{X}\|_F^2 + \lambda \cdot \mathbf{Rank}(\mathbf{X}). \quad (3)$$

However, problem (3) is NP-hard [24] since $\mathbf{Rank}(\cdot)$ is nonconvex and discontinuous. Inspired by compressed sensing [25], $\mathbf{Rank}(\cdot)$ is relaxed to the nuclear norm, leading to the famous nuclear norm minimization (NNM) problem:

$$\arg \min_{\mathbf{X}} \frac{1}{2\sigma_n^2} \|\mathbf{Y} - \mathbf{X}\|_F^2 + \lambda \|\mathbf{X}\|_*, \quad (4)$$

where $\|\mathbf{X}\|_* = \sum_i \sigma_i(\mathbf{X})$, and $\sigma_i(\mathbf{X})$ is the i th leading singular value. In theory, Fazel et al. [26] proved that nuclear norm is the best approximation of the $\mathbf{Rank}(\cdot)$ in all convex functions. Moreover, NNM-based models can be solved efficiently [27]–[29]. Although having theoretical supports and efficient solvers, NNM still has drawbacks. Lots of experiments on image denoising [30]–[32] demonstrate that the results produced by

This work was supported by the Fundamental Research Funds for the Central Universities under Grant SWU-XDJH202303. (Corresponding author: Zhi Wang.)

Yiwen Shan and Dong Hu are with the College of Computer and Information Science, Southwest University, Chongqing 400715, China (e-mail: yvinshan@foxmail.com; donghu@email.swu.edu.cn).

Zhi Wang is with the College of Computer and Information Science, Southwest University, Chongqing 400715, China, and also with the Big Data and Intelligence Engineering School, Chongqing College of International Business and Economics, Chongqing 401520, China (e-mail: chiw@swu.edu.cn).

NNM-based models deviate from the optimal solutions severely. This is attributed to the nuclear norm treating all singular values equally. Consequently, the dominant singular values are over-shrunk during the optimization process. In a nutshell, nuclear norm cannot approximate the rank function with sufficient accuracy, especially in handling inverse problems in image processing. Therefore, a variety of nonconvex surrogates of the rank function have been studied [33]–[38]. In theory, nonconvex surrogates can approximate the rank function better and make the denoising models produce better performance. The famous weighted nuclear norm minimization (WNNM) model [30] assigns different weights to different singular values. In this way, the larger singular values would be shrunk less, and hence the major information would be protected better. This practice makes WNNM outperforms NNM on grayscale image denoising. More importantly, solving WNNM is highly efficient since the global optimum can be obtained in closed-form. However, the performance of WNNM degrades sharply when the noise becomes stronger. That is attributed to the leading singular values still being over-shrunk during the optimization. To further improve the denoising capacity of WNNM, Xie et al. [39] proposed the weighted Schatten p -norm minimization (WSNM) model. WSNM provides more flexible treatments for different rank components. Hence the estimated matrix can be closer to the optimal solution of the rank minimization problem in (3). However, solving WSNM is computationally expensive, since it no longer allow closed-form solutions and have to be solved by numerical algorithms [40].

When denoising color images, the following two challenges have to be considered. First, the data in different color channels has correlations. Second, the noise has not only cross-channel difference but also spatial variation in a single channel. Therefore, the naive strategy that applies grayscale denoisers to each color channel independently cannot obtain satisfactory results since it neglects all those points aforementioned. Three modified strategies can be considered to make low-rank approximation methods feasible for color image denoising. The first is to transform the color image from RGB space into a new color space where channels demonstrate less correlation, and then denoise each channel independently [41]. However, the transformation may complicate the distribution of noise [19]. In addition, the correlation among color channels cannot be fully exploited. The second strategy is to encode color images using more complex data structures, for example, the quaternion [16], [32], [42], in order to preserve the inherent correlation among color channels. However, existing quaternion-based color image denoising methods mostly ignore the cross-channel difference and spatial variation of noise. Moreover, the algorithms converge slowly when solving quaternion-based models. The third strategy is to introduce mutuality between RGB channels and denoise them jointly. Along this line, WNNM and WSNM are respectively extended to color image denoising in [19] and [20]. Their key idea is introducing a weight matrix to characterize the cross-channel difference of noise. However, the extended models inherit the drawbacks from their grayscale version. In addition, both of them ignore the spatial variation of noise.

In summary, as shown in Table I, none of the aforementioned

TABLE I
COMPARISONS AMONG LOW-RANK APPROXIMATION MODELS ON (A): FLEXIBILITY TO DEALING WITH THE CROSS-CHANNEL DIFFERENCE OF NOISE; (B): FLEXIBILITY TO DEALING WITH SPATIALLY VARIANT NOISE; (C): EFFICIENT SOLVER (CAN BE SOLVED VIA A SINGLE ITERATIVE ALGORITHM); (D): THEORETICAL CONVERGENCE GUARANTEE.

Model	Expression	A	B	C	D
LRQA [32]	$\min_{\mathbf{X}} \frac{1}{2} \ \mathbf{Y} - \mathbf{X}\ _F^2 + \lambda \Psi(\mathbf{X})$	×	×	✓	×
MCWNNM [19]	$\min_{\mathbf{X}} \ \mathbf{W}(\mathbf{Y} - \mathbf{X})\ _F^2 + \ \mathbf{X}\ _{w,*}$	✓	×	✓	✓
MCWSNM [20]	$\min_{\mathbf{X}} \ \mathbf{W}(\mathbf{Y} - \mathbf{X})\ _F^2 + \ \mathbf{X}\ _{w,Sp}$	✓	×	✓	✓
NNFNM [21]	$\min_{\mathbf{X}} \ \mathbf{W}(\mathbf{Y} - \mathbf{X})\ _F^2 + \lambda \ \mathbf{X}\ _{t,*-F}$	✓	×	✓	✓
DtNFM (Ours)	$\min_{\mathbf{X}} \ \mathbf{C}(\mathbf{Y} - \mathbf{X})\mathbf{S}\ _F^2 + \lambda \ \mathbf{X}\ _{t,*-F}$	✓	✓	✓	✓

low-rank approximation models obtain (A-B) flexibility to dealing with noise, (C) efficient solver, and (D) theoretical convergence guarantee simultaneously. To fill in this blank, this paper proposes a new low-rank approximation model, called double-weighted truncated nuclear norm minus truncated Frobenius norm minimization (DtNFM), and apply it to color image denoising through exploiting the framework of NSS prior. The proposed DtNFM model has two merits. First, it is flexible in dealing with the noise. Concretely, two weight matrices are designed to respectively model the cross-channel difference and spatial variation of noise. And a heuristic scheme is proposed for adaptively determining the trade-off between two weight matrices. Second, the proposed DtNFM model is flexible in treating different rank components, which guarantees the underlying clean matrix can be estimated with sufficient accuracy. The novelty and contributions of this work are summarized as follows:

- The DtNFM model is proposed and applied to color image denoising. The proposed model possesses sufficient flexibility to deal with the cross-channel difference and spatial variation of noise. Meanwhile, the original clean matrix can be estimated with more accuracy, since its low-rankness obtains a closer approximation.
- To solve the DtNFM model, an efficient algorithm is developed through exploiting the framework of ADMM. Meanwhile, the truncated nuclear norm minus truncated Frobenius norm regularized least squares subproblem is discussed in detail. It is shown that the global optimum can be directly obtained in closed-form rather than transforming the corresponding nonconvex optimization problem into two convex problems [43]. Leveraging on it, the DtNFM model can be efficiently solved by a single ADMM, without nesting other iterative algorithms.
- Theoretical convergence guarantee is obtained, even though the optimization problem resulting from the DtNFM model is nonconvex. Concretely, we prove that the solution sequences generated by our algorithm converge to a single critical point, which indicates our algorithm is capable to solve the DtNFM model.
- To validate the denoising capacity of DtNFM, extensive experiments are carried out on 1) spatially invariant, 2) spatially variant, and 3) real-world noise removal. The results demonstrate that the proposed DtNFM method outperforms state-of-the-art color image denoising methods.

The rest of this paper is organized as follows. Section II

presents the notations and some related works. In Section III, the DtNFM model is proposed. Then, an efficient algorithm is devised and its convergence is analyzed. In Section IV, the experimental results are reported and analyzed. Finally, some conclusions are drawn in Section V.

II. NOTATIONS AND RELATED WORKS

In this section, we summarize the notations used in this paper. Then, we introduce some famous low-rank approximation-based color image denoising methods and the ADMM framework.

A. Notations

In this paper, vectors and matrices are respectively denoted by lowercase boldface and uppercase boldface. \mathbf{I} denotes the identity matrix. For a vector $\mathbf{x} = [x_i] \in \mathbb{R}^m$, $\text{Diag}(\mathbf{x})$ creates a $m \times m$ diagonal matrix with x_i as the i th element of the main diagonal. And $\|\mathbf{x}\|_2 = \sqrt{\sum_{i=1}^n x_i^2}$ is the vector ℓ_2 norm. Given $\mathbf{X}, \mathbf{Y} \in \mathbb{R}^{m \times n}$, $\langle \mathbf{X}, \mathbf{Y} \rangle = \sum_{j=1}^n \sum_{i=1}^m \mathbf{X}_{ij} \times \mathbf{Y}_{ij}$ is their inner product, $\mathbf{X} \oslash \mathbf{Y} \in \mathbb{R}^{m \times n}$ is the Hadamard division, and $[\mathbf{X}; \mathbf{Y}] \in \mathbb{R}^{2m \times n}$ vertically appends matrix \mathbf{Y} to \mathbf{X} . $\|\mathbf{X}\|_* = \sum_i \sigma_i(\mathbf{X})$ is its nuclear norm, where $\sigma_i(\mathbf{X})$ is the i th leading singular value. $\|\mathbf{X}\|_F = \sqrt{\sum_i \sigma_i(\mathbf{X})^2}$ is the Frobenius norm.

B. Color Image Denoising Methods Based on Low-rank Approximation

The multi-channel weighted nuclear norm minimization (MCWNNM) [19] can be formulated as

$$\arg \min_{\mathbf{X} \in \mathbb{R}^{m \times n}} \|\mathbf{W}(\mathbf{Y} - \mathbf{X})\|_F^2 + \|\mathbf{X}\|_{w,*}, \quad (5)$$

where \mathbf{X}, \mathbf{Y} are respectively the estimated patch matrix and the corrupted observation. The weight matrix $\mathbf{W} = \text{Diag}([\sigma_r^{-1}\mathbf{1}; \sigma_g^{-1}\mathbf{1}; \sigma_b^{-1}\mathbf{1}]) \in \mathbb{R}^{m \times m}$ is used to model the cross-channel difference of noise, with σ_c ($c \in \{r, g, b\}$) as the noise standard deviation in channel c . Since $\mathbf{W}_{ii} \propto \sigma_c^{-1}$, the stronger noise will result in the data in this channel providing less contribution to the denoised result. The MCWNNM model pioneers the use of weight matrix, and verifies the effectiveness of the joint denoising strategy. The $\|\mathbf{X}\|_{w,*} = \sum_i w_i \sigma_i(\mathbf{X})$ in (5) is the weighted nuclear norm, where $\{w_i\}$ are determined by some prior knowledge. Benefited from the weights, the larger singular values are shrunk less during the optimization of MCWNNM. Hence the major information can be preserved better. More importantly, it was proved in [31] that the proximal operator of weighted nuclear norm, formulated as

$$\arg \min_{\mathbf{X} \in \mathbb{R}^{m \times n}} \frac{1}{2} \|\mathbf{X} - \mathbf{Y}\|_F^2 + \|\mathbf{X}\|_{w,*}, \quad (6)$$

has a cheap closed-form solution. Therefore, the problem in (5) can be efficiently solved by a single ADMM algorithm, without nesting other iterative algorithms. Nevertheless, MCWNNM inherits the drawback of WNNM that the leading singular values might not be protected well enough, especially in the case of reducing severe noise.

To alleviate this problem, the MCWSNM model [20] is proposed, which can be formulated as

$$\arg \min_{\mathbf{X} \in \mathbb{R}^{m \times n}} \|\mathbf{W}(\mathbf{Y} - \mathbf{X})\|_F^2 + \|\mathbf{X}\|_{w,Sp}^p, \quad (7)$$

where $\|\mathbf{X}\|_{Sp}^p = \sum_i w_i \sigma_i(\mathbf{X})^p$ is the weighted Schatten p -norm. The parameter $p \in (0, 1]$ provides more flexibility to control the shrinkage on singular values. Hence the over-shrinking problem of MCWNNM can be alleviate. However, the proximal operator of the weighted Schatten p -norm has to be solved by iterative algorithms, such as the GST [40]. Consequently, to solve the problem in (7), one has to nest the GST algorithm into the ADMM, which is inefficient. The nuclear norm minus Frobenius norm (NNFN) minimization [21] combines the advantages of MCWNNM and MCWSNM, since the NNFN not only allows closed-form proximal operator, but also have sufficient flexibility on shrinking the singular values. However, the aforementioned methods are not adequate to handle the spatially variant noise, since the weight matrix they use can only model the cross-channel difference of noise.

Recently, lots of quaternion-based methods are proposed for color image denoising [16], [32]. Performing the low-rank approximation in quaternion domain, those methods are able to preserve more correlation among RGB channels. However, modeling the mathematical characters of the noise, such as the cross-channel difference and spatial variation, becomes difficult in the quaternion domain.

C. Alternating Direction Method of Multipliers (ADMM)

The ADMM is an efficient algorithm to solve a wide variety of problems arising in statistics and machine learning. Consider the general regularized optimization problem:

$$\arg \min_{\mathbf{x}} \mathcal{F}(\mathbf{x}) + \lambda \Phi(\mathbf{x}), \quad (8)$$

where $\mathbf{x} \in \mathbb{R}^n$, $\mathcal{F} : \mathbb{R}^n \rightarrow \mathbb{R} \cup \{+\infty\}$ is convex, $\Phi : \mathbb{R}^n \rightarrow \mathbb{R} \cup \{+\infty\}$ is a generic regularizer, $\lambda > 0$ is a parameter. Problem (8) can be rewritten as

$$\min_{\mathbf{x}, \mathbf{z}} \mathcal{F}(\mathbf{x}) + \lambda \Phi(\mathbf{z}) \quad \text{s.t.} \quad \mathbf{x} - \mathbf{z} = \mathbf{0}, \quad (9)$$

where $\mathbf{z} \in \mathbb{R}^n$ is the auxiliary variable, $\mathbf{0} \in \mathbb{R}^n$ is a vector of zeros. The augmented Lagrangian for problem (9) is

$$\mathcal{L}_\rho(\mathbf{x}, \mathbf{z}, \mathbf{y}) = \mathcal{F}(\mathbf{x}) + \lambda \Phi(\mathbf{z}) + \mathbf{y}^\top (\mathbf{x} - \mathbf{z}) + \frac{\rho}{2} \|\mathbf{x} - \mathbf{z}\|_2^2, \quad (10)$$

where $\mathbf{y} \in \mathbb{R}^n$ is the Lagrangian multiplier, and $\rho > 0$ is the penalty parameter. The ADMM minimizes the augmented Lagrangian with respect to \mathbf{x} and \mathbf{z} in an alternative manner:

$$\begin{cases} \mathbf{x}_{k+1} = \arg \min_{\mathbf{x}} \mathcal{L}_\rho(\mathbf{x}, \mathbf{z}_k, \mathbf{y}_k), \\ \mathbf{z}_{k+1} = \arg \min_{\mathbf{z}} \mathcal{L}_\rho(\mathbf{x}_{k+1}, \mathbf{z}, \mathbf{y}_k), \end{cases} \quad (11)$$

$$\mathbf{z}_{k+1} = \arg \min_{\mathbf{z}} \mathcal{L}_\rho(\mathbf{x}_{k+1}, \mathbf{z}, \mathbf{y}_k), \quad (12)$$

where $k \in \mathbb{N}$ denotes the iteration. Then, the Lagrangian multiplier is updated in a feedback manner:

$$\mathbf{y}_{k+1} = \mathbf{y}_k + \rho(\mathbf{x}_{k+1} - \mathbf{z}_{k+1}). \quad (13)$$

Steps (11) ~ (13) are performed until convergence. Albeit the great success of ADMM on convex problems, it is still a great challenge to extend the ADMM to solving nonconvex problems. In particular, the convergence of the ADMM remains as an open issue when the objective becomes nonconvex. Nevertheless, lots of works have shown that ADMM works very well for various nonconvex problems, obtaining satisfactory performance with high efficiency [44]–[48].

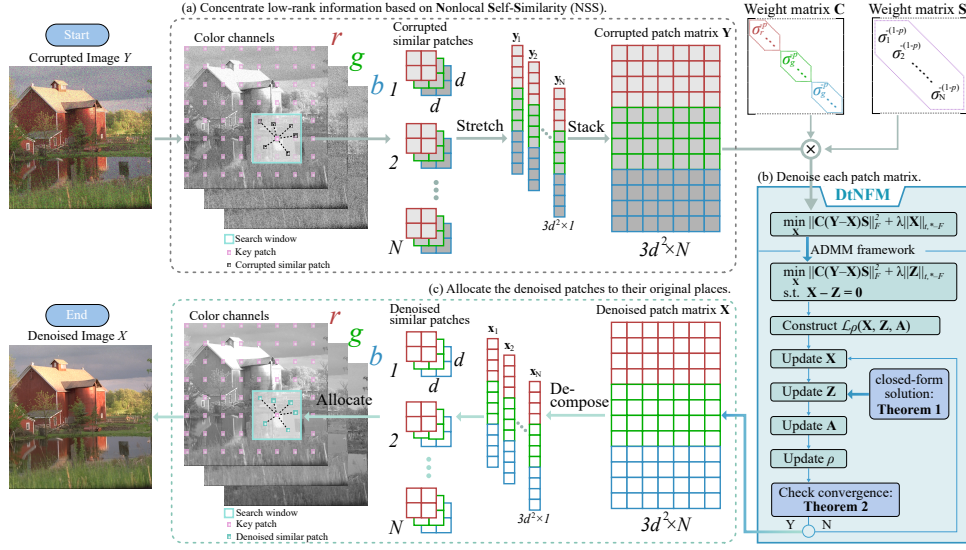


Fig. 1. An overview of our DtNFM method. (a) Group similar patches. For each key patch, the similar patches are found via the k NN algorithm. Those similar patch compose a patch matrix \mathbf{Y} . Using the data in \mathbf{Y} , the weight matrices \mathbf{C} and \mathbf{S} are constructed. (b) Denoise each patch matrix. The matrices \mathbf{Y} , \mathbf{C} and \mathbf{S} are used to formulate the DtNFM model in (14). The generated optimization problem is solved by the proposed Algorithm 2. At each iteration, the variables \mathbf{X} , \mathbf{Z} , \mathbf{A} , and ρ are updated in an alternating manner. (c) Generate the denoised image. The patch matrix \mathbf{X} outputted from DtNFM model is decomposed to patches. Those denoised patches are settled to their original places. After processing all of the P patch matrices, the denoised image is obtained.

III. THE PROPOSED MODEL

In this section, we first decompose the color image denoising problem from the whole image to each patch matrix through exploiting the NSS prior. Then, the DtNFM model is proposed to characterize the denoising problem of each patch matrix. After that, a closed-form proximal operator is proposed for the truncated nuclear norm minus truncated Frobenius norm (tNF) regularizer. Leveraging on it, an efficient algorithm is developed to solve the DtNFM model. Finally, the convergence guarantee of our algorithm is provided.

A. Problem Formulation

The proposed DtNFM method is composed of two parts: 1) patch grouping via exploiting the NSS prior and 2) low-rank approximation by solving the problem resulted by the DtNFM model. The detailed processes are shown in Fig. 1. Given a corrupted color image $Y \in \mathbb{R}^{H \times W \times 3}$, P key patches are assigned across it. The key patches are spaced apart with an equal distance s , and each sizes $d \times d \times 3$ pixels. And hence the number of key patches $P = \lceil (H - d)/s \rceil \times \lceil (W - d)/s \rceil$. For each key patch, its N nearest neighbors, i.e., the most similar patches, are extracted from a search window around it. Those extracted similar patches are then stretched to N column vectors $\mathbf{y}_i \in \mathbb{R}^{3d^2}$, $i \in \{1, \dots, N\}$. The N vectors are stacked horizontally to form a corrupted patch matrix $\mathbf{Y} \in \mathbb{R}^{3d^2 \times N}$. Note that the relationship between key patches and patch matrices is one-to-one. Therefore, P corrupted patch matrices should be constructed in total. Then, the proposed DtNFM model will operate on each of them, estimating its clean version $\mathbf{X} \in \mathbb{R}^{3d^2 \times N}$. After that, \mathbf{X} will be decomposed to N vectors $\mathbf{x}_i \in \mathbb{R}^{3d^2}$, $i \in \{1, \dots, N\}$. For each vector, it will be reshaped back to a denoised patch and then settled to its original place. After processing all of the P denoised patch matrices, the denoised image can be obtained. To obtain better

Algorithm 1: Color image denoising via the DtNFM method.

Input: Corrupted image $Y \in \mathbb{R}^{H \times W \times 3}$, noise standard deviations $[\sigma_{r,0}; \sigma_{g,0}; \sigma_{b,0}]$;
Output: Denoised image $X \in \mathbb{R}^{H \times W \times 3}$;
1 Initialize $X_0 = Y_0 = Y$, θ , s , N ;
2 **for** $l = 1 : \theta$ **do**
3 Iterative regularization $Y_l = X_{l-1} + \delta(Y_0 - X_{l-1})$;
4 Assign P key patches in X_{l-1} ;
5 **for** Each key patch **do**
6 Extract N most similar neighbors to form the patch matrix \mathbf{Y} ;
7 Construct the weight matrices \mathbf{C} and \mathbf{S} ;
8 $\mathbf{X} = \text{DtNFM_model}(\mathbf{Y}, \mathbf{C}, \mathbf{S})$;
9 **end**
10 Aggregate all of P denoised patch matrices to generate X_l ;
11 **end**

results, the procedure above should be repeated θ iterations. The complete procedure of the proposed color image denoising method is summarized in Algorithm 1.

A problem left over from Algorithm 1 is how to estimate the clean patch matrix $\mathbf{X} \in \mathbb{R}^{3d^2 \times N}$ with high accuracy and efficiency. To this end, we propose the DtNFM model, which can be formulated as

$$\arg \min_{\mathbf{X}} \|\mathbf{C}(\mathbf{Y} - \mathbf{X})\mathbf{S}\|_F^2 + \lambda \|\mathbf{X}\|_{t,*-F}, \quad (14)$$

where $\mathbf{C} \in \mathbb{R}^{3d^2 \times 3d^2}$ is the weight matrix to model the cross-channel difference of noise, $\mathbf{S} \in \mathbb{R}^{N \times N}$ is to model the spatial variation of noise. The truncated nuclear norm minus truncated

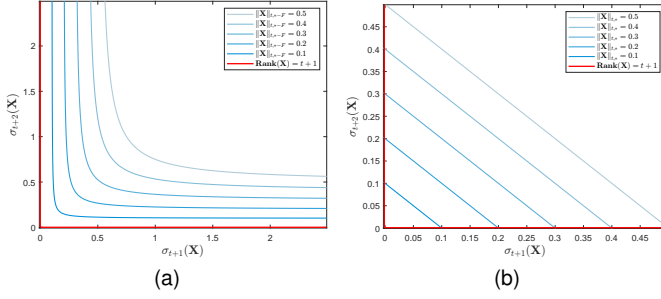


Fig. 2. Contours of the tNF and the truncated nuclear norm. Assume the matrix $\mathbf{X} \in \mathbb{R}^{n \times (t+2)}$ with $n \geq t+2$. As the $\|\mathbf{X}\|_{t,*-F}$ in (a) is minimized from 0.5 to 0.1, its curve approaches to the axes on which $\text{Rank}(\mathbf{X}) = t+1$ holds. Thus the rank of matrix $\mathbf{X} \in \mathbb{R}^{n \times (t+2)}$ will be regularized down to $t+1$. And the low-rankness of \mathbf{X} will be promoted by the tNF minimization. In contrast, the truncated nuclear norm behaves worse than the tNF on promoting the low-rankness.

Frobenius norm (tNF) is defined as

$$\|\mathbf{X}\|_{t,*-F} = \left(\sum_{i=t+1}^{\min(3d^2, N)} \sigma_i(\mathbf{X}) \right) - \alpha \left(\sum_{i=t+1}^{\min(3d^2, N)} \sigma_i(\mathbf{X})^2 \right)^{\frac{1}{2}}, \quad (15)$$

where $t \in \mathbb{N}$ and $\alpha \in [0, +\infty)$ are parameters. Compared with other low-rank approximation based models, the proposed DtNFM model has the following three advantages simultaneously.

- *It is able to deal with the spatially variant noise*, since two weight matrices are used to characterize the noise. The matrix \mathbf{C} is to characterize the noise standard deviations in three color channels, making the DtNFM model able to handle the cross-channel difference of noise. Meanwhile, the DtNFM model can model the noise standard deviations on each of the N neighbor patches using the matrix \mathbf{S} . Hence it has sufficient flexibility in handling the noise variation among patches.

- *It can estimate the underlying low-rank matrix with high accuracy*, since the tNF regularizer can give a close approximation to the rank function. Recap that the estimated patch matrix $\mathbf{X} \in \mathbb{R}^{3d^2 \times N}$ should be of low rank since the N patches constituting it have similar structures. As shown in Fig. 2, compared with other regularizers, tNF has more capacity on promoting the low-rankness and finding low-rank matrices [43]. Furthermore, the tNF has sufficient flexibility on approximating the rank function since its shrinkage on different singular values can be tuned flexibly.

- *It can be solved efficiently by a single iterative algorithm*, since we proved that the proximal operator associated with tNF allows cheap closed-form solution. In previous works [34], [43], such proximal operator has no analytical solution but has to be solved by inefficient iterative algorithms, such as the difference of convex algorithms (DCA) [49]. This drawback restricts the application of many tNF-based models. To this end, we mathematically proved that the global optimum of the proximal operator of tNF can be easily obtained in closed-form. Hence we can directly obtain the solution of problem (33) in a single step. This offers an efficient algorithm to solve the problem in (14).

In the rest of this section, we elaborate the construction of weight matrices \mathbf{C} and \mathbf{S} . Given a corrupted patch matrix

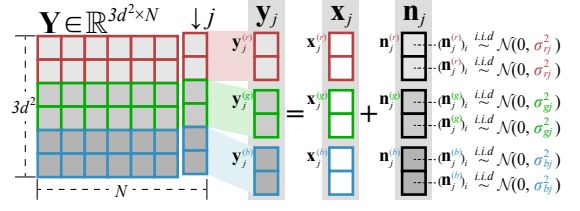


Fig. 3. An illustration of the definitions of \mathbf{y}_j , \mathbf{x}_j , $\mathbf{x}_j^{(c)}$, and \mathbf{n}_j .

$\mathbf{Y} \in \mathbb{R}^{3d^2 \times N}$, as shown in Fig. 3, we denote the j th column as $\mathbf{y}_j = [\mathbf{y}_j^{(r)}; \mathbf{y}_j^{(g)}; \mathbf{y}_j^{(b)}] \in \mathbb{R}^{3d^2}$, where $\mathbf{y}_j^{(c)} \in \mathbb{R}^{d^2}$ is the observed data of channel $c \in \{r, g, b\}$. Correspondingly, define $\mathbf{x}_j = [\mathbf{x}_j^{(r)}; \mathbf{x}_j^{(g)}; \mathbf{x}_j^{(b)}]$, $\mathbf{n}_j = [\mathbf{n}_j^{(r)}; \mathbf{n}_j^{(g)}; \mathbf{n}_j^{(b)}] \in \mathbb{R}^{3d^2}$ as the underlying ground truth data and the noise, respectively. Based on model (1), we have $\mathbf{y}_j = \mathbf{x}_j + \mathbf{n}_j$ and $\mathbf{y}_j^{(c)} = \mathbf{x}_j^{(c)} + \mathbf{n}_j^{(c)}$.

Given the matrix \mathbf{Y} , the original clean matrix can be estimated through exploiting the framework of maximum a-posteriori:

$$\mathbf{X}^* = \arg \max_{\mathbf{X}} P(\mathbf{X}|\mathbf{Y}) = \arg \max_{\mathbf{X}} \ln P(\mathbf{Y}|\mathbf{X}) + \ln P(\mathbf{X}). \quad (16)$$

The likelihood term $P(\mathbf{Y}|\mathbf{X})$ is determined by the statistics of noise. According to [50], we assume the noise is not only independent among RGB channels, but also independent among the similar patches. In other words, we assume $(\mathbf{n}_j^{(c)})_i \stackrel{i.i.d}{\sim} \mathcal{N}(0, \sigma_{cj}^2)$ with $i \in \{1, \dots, d^2\}$, where σ_{cj} is the noise standard deviation in j th patch in channel c . And we define

$$\sigma_{cj} = \sigma_c^p \cdot \sigma_j^{1-p}, \quad (17)$$

where σ_c, σ_j are the noise standard deviations in color channel c and j th patch, respectively, and $p \in [0, 1]$ serves as a relative weight. σ_j is defined as

$$\sigma_j = \left(\left| \frac{\sigma_{r,0}^2 + \sigma_{g,0}^2 + \sigma_{b,0}^2}{3} - \frac{1}{3d^2} \|\mathbf{y}_j - \hat{\mathbf{x}}_j\|_2^2 \right| \right)^{\frac{1}{2}}, \quad (18)$$

where $\sigma_{c,0}$ is the original noise standard deviation in channel $c \in \{r, g, b\}$. In this paper, $\sigma_{c,0}$ is given or can be estimated by off-the-shelf methods [51]. $\hat{\mathbf{x}}_j \in \mathbb{R}^{3d^2}$ is the j th denoised patch output from the previous iteration of Algorithm 1, and is used to estimate the ground truth \mathbf{x}_j in Fig. 3. Before Algorithm 1 iterates, $\hat{\mathbf{x}}_j$ is initialized to \mathbf{y}_j . And σ_c is defined as

$$\sigma_c = \left(\left| \sigma_{c,0}^2 - \frac{1}{d^2} \|\mathbf{y}_j^{(c)} - \hat{\mathbf{x}}_j^{(c)}\|_2^2 \right| \right)^{\frac{1}{2}}. \quad (19)$$

where $\hat{\mathbf{x}}_j^{(c)} \in \mathbb{R}^{d^2}$ is the part of $\hat{\mathbf{x}}_j \in \mathbb{R}^{3d^2}$ in channel c . According to Fig. 3, we have $\hat{\mathbf{x}}_j = [\hat{\mathbf{x}}_j^{(r)}; \hat{\mathbf{x}}_j^{(g)}; \hat{\mathbf{x}}_j^{(b)}]$. And the relative weight p in (17) is determined by

$$p = \frac{v_c + \epsilon}{v_c + v_s + 2\epsilon}, \quad (20)$$

where $v_c, v_s \in \mathbb{R}$ are respectively the coefficient of variation of $[\sigma_r; \sigma_g; \sigma_b]$ and $[\sigma_1, \sigma_2, \dots, \sigma_N]$, and $\epsilon > 0$ is a small value.

After determining σ_{cj} , we can determine $P(\mathbf{Y}|\mathbf{X})$ based on the Gaussian probability density function:

$$P(\mathbf{Y}|\mathbf{X}) = \prod_{j=1}^N \prod_{c \in \{r,g,b\}} \frac{1}{\sqrt{2\pi}\sigma_{cj}} \exp\left(-\frac{\|\mathbf{y}_j^{(c)} - \hat{\mathbf{x}}_j^{(c)}\|_2^2}{2\sigma_{cj}^2}\right), \quad (21)$$

For the estimated patch matrix \mathbf{X} , it is expected to be of low-rank, i.e., the prior probability $P(\mathbf{X}) \propto \exp(-\mathbf{Rank}(\mathbf{X}))$. However, the function $\mathbf{Rank}(\mathbf{X})$ is discontinuous, which would make the optimization problem (16) be NP-hard. Therefore, the tNF ($\|\mathbf{X}\|_{t,*-F}$) is used to give a close approximation to the $\mathbf{Rank}(\mathbf{X})$. Then, the prior probability term is defined as

$$P(\mathbf{X}) = \exp\left(-\frac{\lambda}{2}\|\mathbf{X}\|_{t,*-F}\right), \quad (22)$$

where $\lambda > 0$ is a parameter. Finally, the problem (16) can be deduced as

$$\begin{aligned} & \arg \max_{\mathbf{X}} \ln P(\mathbf{Y}|\mathbf{X}) + \ln P(\mathbf{X}) \\ &= \arg \max_{\mathbf{X}} \sum_{j=1}^N \sum_{c \in \{r,g,b\}} \left(-\frac{1}{2\sigma_{cj}^2} \|\mathbf{y}_j^{(c)} - \hat{\mathbf{x}}_j^{(c)}\|_2^2\right) - \frac{\lambda}{2} \|\mathbf{X}\|_{t,*-F} \\ &= \arg \min_{\mathbf{X}} \sum_{j=1}^N \sigma_j^{-2(1-p)} \sum_{c \in \{r,g,b\}} \sigma_c^{-2p} \|\mathbf{y}_j^{(c)} - \hat{\mathbf{x}}_j^{(c)}\|_2^2 + \lambda \|\mathbf{X}\|_{t,*-F} \\ &= \arg \min_{\mathbf{X}} \sum_{j=1}^N \sigma_j^{-2(1-p)} \|\mathbf{C}(\mathbf{y}_j - \hat{\mathbf{x}}_j)\|_2^2 + \lambda \|\mathbf{X}\|_{t,*-F} \\ &= \arg \min_{\mathbf{X}} \|\mathbf{C}(\mathbf{Y} - \mathbf{X})\mathbf{S}\|_F^2 + \lambda \|\mathbf{X}\|_{t,*-F}, \end{aligned} \quad (23)$$

where $\mathbf{C} = \text{Diag}([\sigma_r^{-p}\mathbf{1}; \sigma_g^{-p}\mathbf{1}; \sigma_b^{-p}\mathbf{1}]) \in \mathbb{R}^{3d^2 \times 3d^2}$, and $\mathbf{S} = \text{Diag}([\sigma_1^{-(1-p)}, \dots, \sigma_N^{-(1-p)}]) \in \mathbb{R}^{N \times N}$. Intuitively, as σ_c becomes larger, the data in color channel c will make less contribution to the estimation of \mathbf{X} . In the same manner, a larger σ_j will reduce the contribution of j th noisy patch when estimating \mathbf{X} .

B. Optimization

To solve the proposed DtNFM model, an efficient and effective algorithm is proposed via exploiting the framework of the ADMM. The original problem (14) can be rewritten as

$$\begin{aligned} & \arg \min_{\mathbf{X}, \mathbf{Z}} \|\mathbf{C}(\mathbf{Y} - \mathbf{X})\mathbf{S}\|_F^2 + \lambda \|\mathbf{Z}\|_{t,*-F}, \\ & \text{s.t. } \mathbf{X} - \mathbf{Z} = \mathbf{0}, \end{aligned} \quad (24)$$

where $\mathbf{Z}, \mathbf{0} \in \mathbb{R}^{3d^2 \times N}$ are the auxiliary variable and a matrix of zeros, respectively. The augmented Lagrangian of problem (24) is

$$\begin{aligned} \mathcal{L}_\rho(\mathbf{X}, \mathbf{Z}, \mathbf{A}) &= \|\mathbf{C}(\mathbf{Y} - \mathbf{X})\mathbf{S}\|_F^2 + \lambda \|\mathbf{Z}\|_{t,*-F} \\ &+ \langle \mathbf{A}, \mathbf{X} - \mathbf{Z} \rangle + \frac{\rho}{2} \|\mathbf{X} - \mathbf{Z}\|_F^2, \end{aligned} \quad (25)$$

where $\mathbf{A} \in \mathbb{R}^{3d^2 \times N}$ is the Lagrangian multiplier, and $\rho > 0$ is the penalty parameter. The proposed algorithm solves the following subproblems alternatively until convergence.

$$\begin{cases} \mathbf{X}_{k+1} = \arg \min_{\mathbf{X}} \mathcal{L}_{\rho_k}(\mathbf{X}, \mathbf{Z}_k, \mathbf{A}_k), \end{cases} \quad (26)$$

$$\begin{cases} \mathbf{Z}_{k+1} = \arg \min_{\mathbf{Z}} \mathcal{L}_{\rho_k}(\mathbf{X}_{k+1}, \mathbf{Z}, \mathbf{A}_k), \end{cases} \quad (27)$$

$$\begin{cases} \mathbf{A}_{k+1} = \mathbf{A}_k + \rho_k(\mathbf{X}_{k+1} - \mathbf{Z}_{k+1}), \end{cases} \quad (28)$$

$$\begin{cases} \rho_{k+1} = \mu \cdot \rho_k, \end{cases} \quad (29)$$

where $k \in \mathbb{N}$ is the iteration number and $\mu > 1$ is a scalar. To drive the algorithm to convergence, equation (29) is used to make the $\rho_k \rightarrow +\infty$ as $k \rightarrow \infty$. In the rest of this section, we detail the subproblems (26) and (27).

For subproblem (26), we have

$$\begin{aligned} \mathbf{X}_{k+1} &= \arg \min_{\mathbf{X}} \|\mathbf{C}(\mathbf{Y} - \mathbf{X})\mathbf{S}\|_F^2 + \lambda \|\mathbf{Z}_k\|_{t,*-F} \\ &+ \langle \mathbf{A}_k, \mathbf{X} - \mathbf{Z}_k \rangle + \frac{\rho_k}{2} \|\mathbf{X} - \mathbf{Z}_k\|_F^2 \\ &= \arg \min_{\mathbf{X}} \|\mathbf{C}(\mathbf{Y} - \mathbf{X})\mathbf{S}\|_F^2 + \frac{\rho_k}{2} \|\mathbf{X} - \mathbf{Z}_k + \frac{1}{\rho_k} \mathbf{A}_k\|_F^2. \end{aligned} \quad (30)$$

This is a standard least squares problem, which has a closed-form solution:

$$\mathbf{X}_{k+1} = (2\mathbf{C}^\top \mathbf{C} \mathbf{Y} \mathbf{S}^\top \mathbf{S} + \rho_k \mathbf{Z}_k - \mathbf{A}_k) \odot (2\mathbf{C}^\top \mathbf{C} \mathbf{1} \mathbf{S}^\top \mathbf{S} + \rho_k \mathbf{1}), \quad (31)$$

where $\mathbf{1} \in \mathbb{R}^{3d^2 \times N}$ is a matrix of ones.

Subproblem (27) can be equivalently rewritten as

$$\mathbf{Z}_{k+1} = \arg \min_{\mathbf{Z}} \frac{1}{2} \|\mathbf{Z} - (\mathbf{X}_{k+1} + \frac{1}{\rho_k} \mathbf{A}_k)\|_F^2 + \frac{\lambda}{\rho_k} \|\mathbf{Z}\|_{t,*-F}. \quad (32)$$

Problem (32) is nonconvex, which is rather difficult to solve by traditional optimization techniques. To address this issue, we propose the following theorem to show that the global optimum of problem (32) can be obtained in closed-form.

Theorem 1. Assume that $\tau > 0$ and $\mathbf{B} \in \mathbb{R}^{m \times n}$ admits SVD as $\mathbf{U}_B \text{Diag}(\boldsymbol{\sigma}(\mathbf{B})) \mathbf{V}_B^\top$, without loss of generality, let $m \geq n$. Then, the closed-form solution to

$$\arg \min_{\mathbf{Z}} \frac{1}{2} \|\mathbf{Z} - \mathbf{B}\|_F^2 + \tau \|\mathbf{Z}\|_{t,*-F}, \quad (33)$$

is given by

$$\mathbf{Z}^* = \mathbf{U}_B \text{Diag}(\boldsymbol{\varrho}^*) \mathbf{V}_B^\top, \quad (34)$$

where

$$\boldsymbol{\varrho}_i^* = \begin{cases} \sigma_i(\mathbf{B}), & \text{if } 0 \leq i < t+1, \\ (1 + \frac{\alpha\tau}{\|\mathcal{S}_\tau(\mathbf{r})\|_2}) \mathcal{S}_\tau(\sigma_i(\mathbf{B})), & \text{if } t+1 \leq i \leq n, \end{cases} \quad (35)$$

where $\mathbf{r} = [0, \dots, 0, \sigma_{t+1}(\mathbf{B}), \dots, \sigma_n(\mathbf{B})]^\top$ and $\mathcal{S}_\tau(\mathbf{r})_i = \max(\mathbf{r}_i - \tau, 0)$ be the soft shrinkage [27].

Proof: Consider \mathbf{Z} admits SVD as $\mathbf{U}_Z \boldsymbol{\Sigma}_Z \mathbf{V}_Z^\top$. The first term of problem (33) can be rewritten as

$$\frac{1}{2} \|\mathbf{Z} - \mathbf{B}\|_F^2 = \frac{1}{2} (\|\mathbf{Z}\|_F^2 - 2\langle \mathbf{Z}, \mathbf{B} \rangle + \|\mathbf{B}\|_F^2). \quad (36)$$

According to Von Neumann's trace inequality, we have

$$\begin{aligned} \langle \mathbf{Z}, \mathbf{B} \rangle &= \text{tr}(\mathbf{Z}^\top \mathbf{B}) = \text{tr}(\mathbf{V}_\mathbf{Z} \Sigma_\mathbf{Z} \mathbf{U}_\mathbf{Z}^\top \mathbf{B}) = \text{tr}(\Sigma_\mathbf{Z} \mathbf{U}_\mathbf{Z}^\top \mathbf{B} \mathbf{V}_\mathbf{Z}) \\ &\leq \sum_{i=1}^n \sigma_i(\mathbf{Z}) \cdot \sigma_i(\mathbf{B}) \cdot \sigma_i(\mathbf{U}_\mathbf{Z}^\top \mathbf{V}_\mathbf{Z}) = \sum_{i=1}^n \sigma_i(\mathbf{Z}) \cdot \sigma_i(\mathbf{B}). \end{aligned} \quad (37)$$

The equality of (37) occurs if and only if

$$\mathbf{U}_\mathbf{Z} = \mathbf{U}_\mathbf{B}, \mathbf{V}_\mathbf{Z} = \mathbf{V}_\mathbf{B}. \quad (38)$$

Therefore, problem (33) can be rewritten as follows:

$$\begin{aligned} &\arg \min_{\mathbf{Z}} \frac{1}{2} \|\mathbf{Z} - \mathbf{B}\|_F^2 + \tau \|\mathbf{Z}\|_{t,*-F} \\ &= \arg \min_{\mathbf{Z}} \frac{1}{2} \|\mathbf{Z}\|_F^2 - \sum_{i=1}^n \sigma_i(\mathbf{Z}) \sigma_i(\mathbf{B}) + \frac{1}{2} \|\mathbf{B}\|_F^2 \\ &\quad + \tau \left(\sum_{i=t+1}^n \sigma_i(\mathbf{Z}) - \alpha \left(\sum_{i=t+1}^n \sigma_i(\mathbf{Z})^2 \right)^{\frac{1}{2}} \right) \\ &= \arg \min_{\mathbf{Z}} \sum_{i=1}^t \left(\frac{1}{2} \sigma_i(\mathbf{Z})^2 - \sigma_i(\mathbf{Z}) \sigma_i(\mathbf{B}) \right) + \sum_{i=t+1}^n \left(\frac{1}{2} \sigma_i(\mathbf{Z})^2 \right. \\ &\quad \left. - \sigma_i(\mathbf{Z}) \sigma_i(\mathbf{B}) + \tau \sigma_i(\mathbf{Z}) \right) - \alpha \tau \left(\sum_{i=t+1}^n \sigma_i(\mathbf{Z})^2 \right)^{\frac{1}{2}}. \end{aligned} \quad (39)$$

Therefore, the original problem (33) has been equivalently transformed into the combination of independent quadratic equations for each $\sigma_i(\mathbf{Z})$. Let $F(\sigma(\mathbf{Z}))$ denote the objective function of (39). The minimum of F , denoted as ϱ_i^* , is given by

$$\frac{\partial F}{\partial \sigma_i(\mathbf{Z})} = 0. \quad (40)$$

When $0 \leq i < t+1$, it is trivial to obtain

$$\varrho_i^* = \sigma_i(\mathbf{B}). \quad (41)$$

When $t+1 \leq i \leq n$, equation (40) is expressed as

$$\left(1 - \frac{\alpha \tau}{\sqrt{\sum_{i=t+1}^n (\varrho_i^*)^2}} \right) \varrho_i^* = \sigma_i(\mathbf{B}) - \tau. \quad (42)$$

And the solution of (42) is

$$\varrho_i^* = \left(1 + \frac{\alpha \tau}{\|\mathcal{S}_\tau(\mathbf{r})\|_2} \right) \cdot \mathcal{S}_\tau(\sigma_i(\mathbf{B})), \quad (43)$$

where $\mathbf{r} = [0, \dots, 0, \sigma_{t+1}(\mathbf{B}), \dots, \sigma_T(\mathbf{B})]^\top \in \mathbb{R}^n$ and $(\mathcal{S}_\tau(\mathbf{r}))_i = \max(\mathbf{r}_i - \tau, 0)$. Combining (41) and (43), we have

$$\varrho_i^* = \begin{cases} \sigma_i(\mathbf{B}), & \text{if } 0 \leq i < t+1, \\ \left(1 + \frac{\alpha \tau}{\|\mathcal{S}_\tau(\mathbf{r})\|_2} \right) \mathcal{S}_\tau(\sigma_i(\mathbf{B})), & \text{if } t+1 \leq i \leq n. \end{cases} \quad (44)$$

And the optimal solution of problem (33) is

$$\mathbf{Z}^* = \mathbf{U}_\mathbf{B} \text{Diag}(\varrho^*) \mathbf{V}_\mathbf{B}^\top. \quad (45)$$

According to Theorem 1, the global optimum of subproblem (27) is given by (34) and (35), where $\mathbf{B} = \mathbf{X}_{k+1} + \rho_k^{-1} \mathbf{A}_k$ and $\tau = \lambda / \rho_k$. Up to now, the global optima of both subproblem (26) and (27) have been obtained in closed-form.

The algorithm would be terminated when the iteration number exceeds a threshold K or the following stopping

Algorithm 2: Solving problem (14) via ADMM.

Input: corrupted matrix $\mathbf{Y} \in \mathbb{R}^{3d^2 \times N}$, weight matrix $\mathbf{C} \in \mathbb{R}^{3d^2 \times 3d^2}$, $\mathbf{S} \in \mathbb{R}^{N \times N}$;
Output: Denoised matrix $\mathbf{X} \in \mathbb{R}^{3d^2 \times N}$;
1 Initialize $\mathbf{X}_0 = \mathbf{Z}_0 = \mathbf{A}_0 = \mathbf{0}$, $\rho_0, t, \lambda, \mu, \epsilon, k = 0, K$;
2 **while** *Stopping criterion is not satisfied* **do**
3 $\mathbf{X}_{k+1} \leftarrow (2\mathbf{C}^2 \mathbf{Y} \mathbf{S}^2 + \rho_k \mathbf{Z}_k - \mathbf{A}_k) \odot (2\mathbf{C}^2 \mathbf{1} \mathbf{S}^2 + \rho_k \mathbf{1})$;
4 $\mathbf{Z}_{k+1} \leftarrow \arg \min_{\mathbf{Z}} \frac{1}{2} \|\mathbf{Z} - (\mathbf{X}_{k+1} + \frac{1}{\rho_k} \mathbf{A}_k)\|_F^2 + \lambda / \rho_k \|\mathbf{Z}\|_{t,*-F}$;
5 $\mathbf{A}_{k+1} \leftarrow \mathbf{A}_k + \rho_k (\mathbf{X}_{k+1} - \mathbf{Z}_{k+1})$;
6 $\rho_{k+1} \leftarrow \mu \cdot \rho_k$;
7 Check the stopping criterion:
 $((k \leftarrow k+1) > K) \vee (\|\mathbf{X}_{k+1} - \mathbf{Z}_{k+1}\|_F \leq \epsilon) \& \& (\|\mathbf{Z}_{k+1} - \mathbf{Z}_k\|_F \leq \epsilon) \& \& (\|\mathbf{X}_{k+1} - \mathbf{X}_k\|_F \leq \epsilon)$;
8 **end**

criteria hold simultaneously: (a) $\|\mathbf{X}_{k+1} - \mathbf{Z}_{k+1}\|_F \leq \epsilon$, (b) $\|\mathbf{X}_{k+1} - \mathbf{X}_k\|_F \leq \epsilon$, (c) $\|\mathbf{Z}_{k+1} - \mathbf{Z}_k\|_F \leq \epsilon$, where $\epsilon > 0$ is a small tolerance. This stopping criterion is devised based on the convergence guarantee given by Theorem 2. Finally, the complete algorithm for solving problem (14) is summarized in Algorithm 2.

C. Convergence and Complexity Analysis

In this section, we give the following theorem to establish the weak convergence result of Algorithm 2, which facilitates the construction of a reasonable termination condition. The detailed proof can be found in the supplementary material.

Theorem 2. *The sequences $\{\mathbf{X}_k\}$ and $\{\mathbf{Z}_k\}$ generated from Algorithm 2 satisfy*

$$\begin{aligned} (a) \quad &\lim_{k \rightarrow \infty} \|\mathbf{X}_{k+1} - \mathbf{Z}_{k+1}\|_F = 0. \\ (b) \quad &\lim_{k \rightarrow \infty} \|\mathbf{X}_{k+1} - \mathbf{X}_k\|_F = 0. \\ (c) \quad &\lim_{k \rightarrow \infty} \|\mathbf{Z}_{k+1} - \mathbf{Z}_k\|_F = 0. \end{aligned}$$

Theorem 2 guarantees that $\{\mathbf{X}_k\}$ and $\{\mathbf{Z}_k\}$ converge to a single critical point, i.e., $\lim_{k \rightarrow \infty} \mathbf{X}_k = \lim_{k \rightarrow \infty} \mathbf{Z}_k = \mathbf{X}^*$. This converged solution proves that the proposed Algorithm 2 is capable of solving the problem resulted by the DtNFM model in (14).

The time complexity of Algorithm 2 is discussed in brief. In step 3, updating $\mathbf{X} \in \mathbb{R}^{3d^2 \times N}$ takes $\mathcal{O}(d^4 N)$ time. In step 4, the complexity is $\mathcal{O}(d^2 N^2 + d^4 N)$ since the SVD of $\mathbf{X}_{k+1} + \rho_k^{-1} \mathbf{A}_k \in \mathbb{R}^{3d^2 \times N}$ costs $\mathcal{O}(d^2 N^2)$ time. The complexity of step 5 is $\mathcal{O}(d^2 N)$. Therefore, the complexity of Algorithm 2 is $\mathcal{O}((d^4 N + d^2 N^2)K)$. In Algorithm 1, step 6 costs $\mathcal{O}(S^2 \log S)$ time, where $S \in \mathbb{N}_+$ is the side length of the search window. In step 7, constructing $\mathbf{C} \in \mathbb{R}^{3d^2 \times 3d^2}$ and $\mathbf{S} \in \mathbb{R}^{N \times N}$ costs $\mathcal{O}(d^4 + N^2)$ time. The dominant cost lies in step 8, which is actually the Algorithm 2. In summary, the complexity of Algorithm 1 is $\mathcal{O}((d^4 N + d^2 N^2)K P \theta)$.

D. Differences From Existing Methods

In this section, we discuss the difference between the proposed DtNFM and three highly related methods—EBD

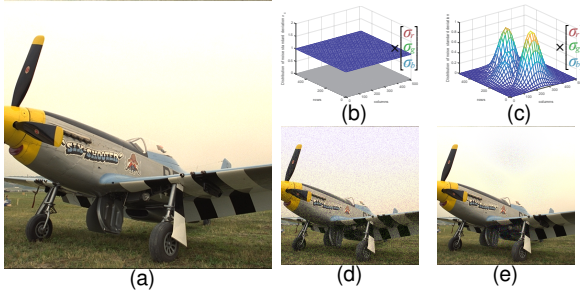


Fig. 4. Illustrations of the spatially invariant noise and the spatially variant noise. (a) the ground truth image “kodim20”. (b) The surface of the standard deviation of spatially invariant noise. (c) The surface of the standard deviation of spatially variant noise, which is returned by MATLAB code “abs(peaks(512))”. A point (x, y, z) means the pixel at x th row and y th column has Gaussian noise with standard deviations being $z \times [\sigma_{r_0}; \sigma_{g_0}; \sigma_{b_0}]$, where $z \in [0, 1]$. Specifically, $z \equiv 1$ in the subfigure (b). (d) The image corrupted by the noise in subfigure (b) with $[\sigma_{r_0}; \sigma_{g_0}; \sigma_{b_0}] = [30; 10; 50]$. (e) The image corrupted by the noise in subfigure (c) with $[\sigma_{r_0}; \sigma_{g_0}; \sigma_{b_0}] = [30; 35; 40]$.

[15], SSLRDM [17], and DLRQP [16]. All of those methods, together with our DtNFM, are based on low-rank approximation, and exploit the NSS prior for image denoising.

First, the proposed DtNFM method is able to handle the spatially variant noise, since a dedicated weight matrix is devised to model the spatial variation of the noise. In contrast, the EBD, SSLRDM and DLRQP can only deal with the spatially invariant noise. Second, the DtNFM method can deal with the difference of the noise among RGB channels. While the DLRQP cannot model this cross-channel difference of noise. And the EBD and SSLRDM are not developed for color image denoising. Third, the algorithm for the DtNFM model possess theoretical convergence guarantee. In contrast, it is difficult to prove the convergence of the algorithm for the DLRQP model, since it incorporates a deep learning denoiser which is effectively a black box. In summary, the proposed DtNFM method has significant difference with those related methods.

IV. EXPERIMENTAL RESULTS AND ANALYSIS

To test the performance of the proposed DtNFM method, three kinds of experiments are conducted, i.e., spatially invariant noise removal, spatially variant noise removal, and real-world noise removal. Nine state-of-the-art methods are compared, including (1) CBM3D [41], (2) DRUNet [12], (3) Restormer [52], (4) HLTA-GN [18], (5) NGmeet [53], (6) DLRQP [16], (7) MCWNNM [19], (8) MCWSNM [20], and (9) NNFNM [21]. The parameters of compared methods are either tuned to the optimum or kept the same as the original codes. The experiments are implemented on a laptop with 2.1GHz CPU, 16GB RAM, and Nvidia GeForce MX350 GPU. The Restormer [52] is trained on a server with 2.1GHz CPU, 64G RAM, and Tesla T4 GPU.

A. Spatially Invariant Noise Removal

The spatially invariant noise removal experiments are carried out on the Kodak24 dataset¹. It includes 24 noise-free color images, as shown in Fig. 5(a). The noise is synthetic, spatially



Fig. 5. The ground truth images of the two dataset (enumerated from left-to-right and top-to-bottom).

invariant, but has cross-channel difference, as shown in Fig. 4(b). The corrupted images are generated by zero-mean Gaussian noise with standard deviation $[\sigma_{r_0}; \sigma_{g_0}; \sigma_{b_0}] \in \{[20; 35; 5], [30; 10; 50]\}$. For CBM3D, NGmeet and DLRQP, a single noise standard deviation should be given for denoising, which is set as

$$\sigma = \sqrt{(\sigma_{r_0}^2 + \sigma_{g_0}^2 + \sigma_{b_0}^2)/3}. \quad (46)$$

Formula (46) is also used to calculate the training noise levels for the Restormer. The parameter settings of the proposed DtNFM method are listed in Table V(a) and Table V(b).

Table II and Table III display the PSNR and SSIM results of all competing methods. The best results are accentuated in bold. Under the noise $[\sigma_{r_0}; \sigma_{g_0}; \sigma_{b_0}] = [20; 35; 5]$, the proposed DtNFM method achieves the highest PSNR on 22 out of 24 images, and the highest SSIM on 23 images. Under the noise $[\sigma_{r_0}; \sigma_{g_0}; \sigma_{b_0}] = [30; 10; 50]$, The proposed DtNFM achieves the highest PSNR and SSIM on all of the 24 images. Focusing on the averages, we list the improvements of DtNFM over other methods at Table IV(a) and Table IV(b). As can be seen, DtNFM achieves higher PSNR and SSIM over the state-of-the-art deep learning methods, i.e., DRUNet and Restormer. DtNFM also outperforms its state-of-the-art counterparts, i.e., MCWNNM, MCWSNM and NNFNM. In terms of running times, the deep learning methods are significantly faster than the proposed DtNFM. However, please note that only their testing time is taken into account, and the training time is not considered. In contrast, the proposed DtNFM method does not have the process of training.

The visual comparisons are shown in Fig. 6 ~ Fig. 8. We can find that the Restormer remains too much noise in the green channel (Fig. 6(e)) or in the blue channel (Fig. 7(e) and Fig. 8(e)). That is because it is inadequate to handle the cross-channel difference of the noise. In Fig. 7, DtNFM achieves better protection on the complex edges of trees and shrub. In contrast, the CBM3D, DRUNet and NGmeet over-smooth the image. The Restormer and DLRQP remains many blue

¹<http://r0k.us/graphics/kodak/>

TABLE II
PSNR AND SSIM RESULTS FOR ALL COMPETING METHODS UNDER $[\sigma_{r_0}; \sigma_{g_0}; \sigma_{b_0}] = [20; 35; 5]$. RUNNING TIME IS IN SECONDS.

#	CBM3D PSNR SSIM	DRUNet PSNR SSIM	Restormer PSNR SSIM	HLTA-GN PSNR SSIM	NGMeet PSNR SSIM	DLRQP PSNR SSIM	MCWNNM PSNR SSIM	MCWSNM PSNR SSIM	NNFNM PSNR SSIM	DtNFM PSNR SSIM
1	28.66 0.8267	29.25 0.8537	25.59 0.7935	28.42 0.8139	28.13 0.8013	28.67 0.8266	31.08 0.8999	31.11 0.903	31.29 0.9057	31.46 0.9147
2	31.53 0.7683	32.81 0.8334	25.02 0.6168	31.59 0.7980	31.47 0.7824	31.06 0.7788	33.76 0.8540	34.02 0.8682	34.05 0.8678	34.22 0.8761
3	33.16 0.8454	34.75 0.9142	23.57 0.6603	33.08 0.8632	33.83 0.8922	32.35 0.8644	35.46 0.9004	35.96 0.9223	36.33 0.9252	36.15 0.9275
4	31.71 0.8017	33.04 0.8561	23.76 0.6480	32.08 0.8308	31.98 0.8213	31.10 0.7966	34.32 0.8795	34.60 0.8922	34.71 0.8941	34.82 0.9001
5	29.17 0.8657	30.64 0.8994	27.67 0.8359	27.73 0.8457	29.10 0.8623	29.49 0.8730	31.12 0.9159	31.23 0.9227	31.29 0.9251	31.35 0.9289
6	29.98 0.8251	30.22 0.8606	25.80 0.7579	29.83 0.8313	29.73 0.8207	29.32 0.8159	32.29 0.8925	32.45 0.9016	32.54 0.9057	32.75 0.9122
7	32.30 0.8749	34.96 0.9439	24.25 0.7330	32.31 0.8944	33.34 0.9228	30.05 0.8767	34.64 0.9229	35.02 0.9401	35.00 0.9378	35.05 0.9428
8	29.27 0.8766	30.45 0.9027	28.01 0.8590	28.72 0.8793	29.28 0.8749	29.10 0.8780	31.19 0.9214	31.28 0.9269	31.28 0.9243	31.11 0.9300
9	32.69 0.8445	34.66 0.9117	23.24 0.6733	32.72 0.8662	33.36 0.8909	31.35 0.8622	34.86 0.8980	35.27 0.9164	35.33 0.9136	35.37 0.9187
10	32.54 0.8382	34.61 0.9093	23.46 0.6792	32.64 0.8638	33.12 0.8747	30.86 0.8347	34.67 0.8954	35.07 0.9115	35.12 0.9099	35.15 0.9153
11	30.54 0.8066	31.43 0.8453	25.10 0.7028	30.17 0.8170	30.32 0.8020	29.79 0.7960	32.53 0.8770	32.70 0.8873	32.76 0.8906	32.94 0.8969
12	32.52 0.8082	33.31 0.8646	23.65 0.6495	33.02 0.8373	32.67 0.8268	31.57 0.8070	34.74 0.8769	35.14 0.8941	35.22 0.8955	35.29 0.9015
13	27.44 0.8082	27.84 0.8201	26.16 0.7758	26.25 0.7722	26.82 0.7622	26.20 0.7820	29.25 0.8875	29.27 0.8875	29.41 0.8940	29.76 0.9053
14	29.46 0.8023	30.50 0.8348	25.72 0.7403	28.49 0.7966	29.28 0.7895	31.47 0.8137	31.78 0.8840	31.87 0.8885	31.95 0.8913	32.14 0.8982
15	32.05 0.8120	31.64 0.8668	25.93 0.7222	32.29 0.8438	32.38 0.8488	30.82 0.8246	34.31 0.8829	34.64 0.9006	34.64 0.8986	34.68 0.9066
16	31.41 0.8159	32.42 0.8648	23.47 0.6504	31.66 0.8304	31.38 0.8241	31.23 0.8175	33.86 0.8861	34.11 0.8996	34.35 0.9040	34.51 0.9098
17	31.83 0.8301	32.77 0.8820	24.59 0.7039	31.25 0.8539	32.08 0.8566	31.20 0.8405	34.08 0.8961	34.39 0.9100	34.48 0.9107	34.57 0.9147
18	29.33 0.8109	30.06 0.8438	25.99 0.7210	27.45 0.7688	28.86 0.7972	29.05 0.8089	31.16 0.8795	31.26 0.8856	31.35 0.8888	31.60 0.8948
19	31.00 0.8147	31.97 0.8591	25.23 0.6764	31.11 0.8311	31.08 0.8256	31.08 0.8251	33.23 0.8863	33.41 0.8969	33.49 0.8983	33.60 0.9059
20	32.35 0.8248	29.80 0.8960	26.58 0.8014	32.62 0.8659	32.61 0.8653	30.50 0.8473	34.27 0.9008	34.69 0.9162	34.29 0.9197	34.25 0.9229
21	30.34 0.8376	31.34 0.8904	24.46 0.7154	30.08 0.8501	30.14 0.8619	28.18 0.8264	32.48 0.8974	32.67 0.9106	32.62 0.9096	33.01 0.9162
22	30.25 0.7829	30.89 0.8227	24.20 0.6366	30.34 0.8036	30.18 0.7846	30.23 0.7865	32.31 0.8645	32.44 0.8733	32.56 0.8761	32.66 0.8842
23	33.26 0.8413	35.34 0.9185	23.37 0.6489	33.83 0.8819	34.45 0.9013	31.47 0.8665	35.53 0.9006	36.06 0.9216	35.97 0.9182	36.14 0.9241
24	29.57 0.8358	30.49 0.8867	26.48 0.7600	28.64 0.8410	29.66 0.8439	29.71 0.8446	31.73 0.8996	31.90 0.9093	31.65 0.9072	31.97 0.9174
Avg.	30.93 0.8249	31.88 0.8742	25.05 0.7151	30.68 0.8367	31.05 0.8389	30.18 0.8289	33.11 0.8916	33.36 0.9036	33.40 0.9047	33.52 0.9110
Time	7.69	2.99	1.54	325.54	529.19	847.17	706.41	867.08	570.86	582.13

TABLE III
PSNR AND SSIM RESULTS FOR ALL COMPETING METHODS UNDER $[\sigma_{r_0}; \sigma_{g_0}; \sigma_{b_0}] = [30; 10; 50]$. RUNNING TIME IS IN SECONDS.

#	CBM3D PSNR SSIM	DRUNet PSNR SSIM	Restormer PSNR SSIM	HLTA-GN PSNR SSIM	NGMeet PSNR SSIM	DLRQP PSNR SSIM	MCWNNM PSNR SSIM	MCWSNM PSNR SSIM	NNFNM PSNR SSIM	DtNFM PSNR SSIM
1	26.90 0.7496	27.11 0.7662	23.81 0.6980	27.60 0.7835	26.44 0.7174	26.52 0.7395	28.81 0.8340	28.86 0.8316	29.01 0.8388	29.55 0.8579
2	30.27 0.7276	29.29 0.7622	26.45 0.6791	30.75 0.7721	30.40 0.7526	29.15 0.7227	31.81 0.7990	31.95 0.8063	32.07 0.8091	32.42 0.8223
3	31.56 0.8038	31.50 0.8683	24.29 0.6574	31.97 0.8332	31.94 0.8510	30.41 0.8208	33.89 0.8752	34.07 0.8886	34.37 0.8928	34.77 0.9030
4	30.22 0.7546	30.76 0.8033	24.43 0.6194	31.02 0.7993	30.37 0.7775	29.11 0.7432	32.26 0.8322	32.39 0.8381	32.60 0.8434	32.96 0.8556
5	27.14 0.8010	27.96 0.8279	24.93 0.7672	26.47 0.8066	26.92 0.7878	26.87 0.7960	29.01 0.8703	29.13 0.8723	29.07 0.8756	29.89 0.8943
6	28.27 0.7650	28.39 0.7899	23.67 0.6486	28.89 0.8018	27.96 0.7503	27.74 0.7425	30.23 0.8388	30.31 0.8413	30.40 0.8520	31.03 0.8675
7	30.61 0.8438	31.74 0.9111	24.44 0.6878	30.69 0.8714	31.18 0.8898	28.79 0.8472	32.81 0.9048	33.02 0.9173	32.93 0.9121	33.62 0.9262
8	27.31 0.8340	28.23 0.8601	24.45 0.7823	27.54 0.8543	27.54 0.8378	26.44 0.8180	29.07 0.8838	29.25 0.8867	29.10 0.8884	29.87 0.9003
9	31.20 0.8139	32.52 0.8794	23.90 0.5937	31.63 0.8418	31.59 0.8610	29.38 0.8185	33.23 0.8729	33.47 0.8873	33.57 0.8854	34.04 0.8982
10	30.96 0.7976	32.44 0.8683	23.91 0.6015	31.43 0.8362	31.26 0.8364	28.87 0.7815	33.00 0.8649	33.19 0.8767	33.24 0.8758	33.88 0.8921
11	28.89 0.7478	28.86 0.7643	24.06 0.6278	29.20 0.7868	28.44 0.7341	28.30 0.7308	30.60 0.8239	30.72 0.8249	30.71 0.8339	31.28 0.8454
12	31.25 0.7695	31.42 0.7997	23.27 0.5678	32.13 0.8145	31.16 0.7887	29.75 0.7615	33.03 0.8379	33.16 0.8452	33.28 0.8515	33.70 0.8623
13	25.45 0.7100	25.51 0.6984	23.58 0.6942	25.05 0.7228	24.68 0.6427	25.38 0.7233	27.07 0.8094	27.25 0.8049	27.19 0.8152	27.88 0.8360
14	27.68 0.7307	28.09 0.7490	24.54 0.6744	27.44 0.7592	27.61 0.7167	27.41 0.7169	29.57 0.8193	29.61 0.8155	29.71 0.8241	30.28 0.8414
15	30.62 0.7746	29.92 0.8271	25.85 0.7191	31.24 0.8136	30.79 0.8095	29.23 0.7871	32.48 0.8446	32.73 0.8567	32.72 0.8577	33.14 0.8706
16	29.91 0.7607	30.30 0.7953	23.32 0.5782	30.73 0.8008	29.77 0.7631	29.35 0.7433	32.02 0.8402	32.04 0.8439	32.38 0.8554	32.81 0.8690
17	30.27 0.7899	29.98 0.8276	24.62 0.6892	30.03 0.8240	30.43 0.8212	28.23 0.7687	32.28 0.8636	32.42 0.8696	32.51 0.8731	33.05 0.8855
18	27.54 0.7386	27.60 0.7664	24.67 0.6958	26.30 0.7210	27.07 0.7231	27.01 0.7209	29.33 0.8202	29.42 0.8230	29.47 0.8287	30.12 0.8483
19	29.51 0.7655	30.00 0.7961	24.05 0.6207	30.20 0.8064	29.75 0.7820	28.22 0.7420	31.54 0.8432	31.56 0.8458	31.74 0.8526	32.15 0.8650
20	30.91 0.7973	28.00 0.8574	24.74 0.7716	31.44 0.8386	31.26 0.8387	28.90 0.8116	32.47 0.8585	32.85 0.8740	32.30 0.8837	32.92 0.8873
21	28.62 0.7954	29.23 0.8409	23.80 0.6379	29.01 0.8201	28.34 0.8128	26.40 0.7621	30.42 0.8561	30.60 0.8665	30.54 0.8667	31.20 0.8812
22	28.80 0.7220	29.07 0.7521	24.05 0.6026	29.49 0.7734	28.23 0.7015	28.08 0.6953	30.47 0.8101	30.51 0.8102	30.69 0.8186	31.11 0.8335
23	31.89 0.8194	32.08 0.8916	25.32 0.6907	32.50 0.8597	32.38 0.8776	30.50 0.8579	33.68 0.8776	34.01 0.8942	33.93 0.8880	34.49 0.9030
24	27.72 0.7739	27.99 0.8171	24.03 0.7087	27.44 0.8074	27.70 0.7796	27.16 0.7615	29.57 0.8531	29.76 0.8585	29.38 0.8543	30.40 0.8810
Avg.	29.31 0.7744	29.50 0.8133	24.34 0.6672	29.59 0.8062	29.30 0.7855	28.22 0.7672	31.19 0.8472	31.34 0.8533	31.37 0.8574	31.94 0.8720
Time	4.92	2.53	1.59	402.94	489.4	581.63	766.43	973.67	583.24	708.87

spots in their denoised results. In Fig. 8, both the textures of the sculpture and the detailed structure of the stone are well recovered by DtNFM. In contrast, the HLTA-GN generates some wrinkle texture, the NGmeet and DLRQP over-smooth the image. In summary, the proposed DtNFM method achieves the best performance in both numerical results and visual quality.

B. Spatially Variant Noise Removal

In the most previous section, the synthetic noise is spatially invariant. However, in practical applications, the noise does demonstrate spatial variation in most cases. Therefore, in this

section we consider the noise possessing both cross-channel difference and spatial variation. To synthesize such kind of noise, we first choose the upper-bounds of the noise standard deviation, denoted as $[\sigma_{r_0}; \sigma_{g_0}; \sigma_{b_0}]$. Then, we generate a map $\mathcal{M}(x, y)$ where $x, y \in \{1, \dots, 512\}$, as shown in Fig. 4(c). Note that $\mathcal{M}(\cdot, \cdot) \in [0, 1]$. A point $(x, y, \mathcal{M}(x, y))$ means that for the pixel at x th row and y th column, the noise standard deviation imposed on it is $\mathcal{M}(x, y) \times [\sigma_{r_0}; \sigma_{g_0}; \sigma_{b_0}]$. For all competing methods, the input noise standard deviation in

TABLE IV
AVERAGE IMPROVEMENTS (PSNR AND SSIM) OF DtNFM OVER OTHER METHODS.

	CBM3D	DRUNet	Restormer	HLTA-GN	NGMeet	DLRQP	MCWNNM	MCWSNM	NNFNM
(a) [20, 35, 5]	2.59 0.0861	1.64 0.0368	8.47 0.196	2.84 0.0744	2.47 0.0721	3.34 0.0821	0.41 0.0194	0.17 0.0074	0.12 0.0064
(b) [30, 10, 50]	2.63 0.0975	2.44 0.0586	7.6 0.2047	2.35 0.0658	2.64 0.0864	3.73 0.1048	0.75 0.0247	0.60 0.0187	0.57 0.0146
(c) Spatially variant noise	2.81 0.0274	2.69 0.0323	1.41 0.0115	2.86 0.0345	0.89 0.0141	2.8 0.0259	2.34 0.0269	3.03 0.0578	2.94 0.0371
(d) Real-world noise	3.71 0.0723	0.35 0.0033	2.02 0.0232	1.4 0.0129	0.87 0.0088	1.41 0.0165	0.56 0.0061	0.72 0.0076	0.06 2.03E-5

TABLE V
PARAMETERS OF THE PROPOSED DtNFM METHOD WITH RESPECT TO FOUR EXPERIMENTS.

	θ	N	d	s	K	t	α	λ	ρ_0	μ
(a) [20, 35, 5]	3	60	6	5	10	2	1.80	0.80	0.30	1.002
(b) [30, 10, 50]	2	60	6	5	10	2	1.80	1.00	0.50	1.002
(c) Spatially variant noise	—	60	4	3	10	2	1.50	0.80	0.45	1.002
(d) Real-world noise	—	60	6	5	10	0	2.00	2.30	0.90	1.002

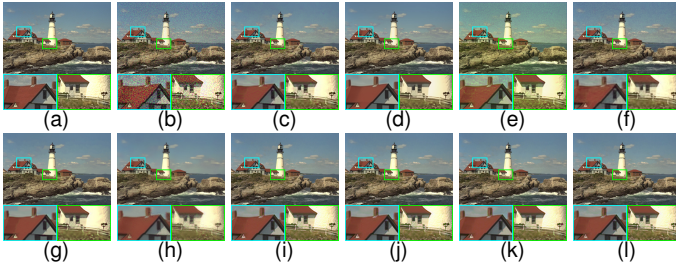


Fig. 6. Denoised results on “kodim21” ($[\sigma_{r,0}; \sigma_{g,0}; \sigma_{b,0}] = [20; 35; 5]$). (a) Ground truth. (b) Noisy observation (20.73, 0.5010). (c) CBM3D (30.34, 0.8376). (d) DRUNet (31.34, 0.8904). (e) Restormer (24.46 0.7154). (f) HLTA-GN (30.08, 0.8501). (g) NGMeet (30.14, 0.8619). (h) DLRQP (28.18, 0.8264). (i) MCWNNM (32.48, 0.8974). (j) MCWSNM (32.67, 0.9106). (k) NNFNM (32.62, 0.9096). (l) DtNFM (**33.01, 0.9162**).

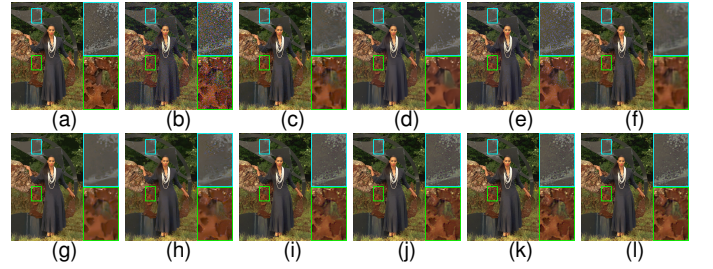


Fig. 8. Denoised results on “kodim18” ($[\sigma_{r,0}; \sigma_{g,0}; \sigma_{b,0}] = [30; 10; 50]$). (a) Ground truth. (b) Noisy observation (17.46, 0.3967). (c) CBM3D (27.54, 0.7386). (d) DRUNet (27.60, 0.7664). (e) Restormer (24.67, 0.6958). (f) HLTA-GN (26.30, 0.7210). (g) NGMeet (27.07, 0.7231). (h) DLRQP (27.01, 0.7209). (i) MCWNNM (29.33, 0.8202). (j) MCWSNM (29.42, 0.8230). (k) NNFNM (29.47, 0.8287). (l) DtNFM (**30.12, 0.8483**).

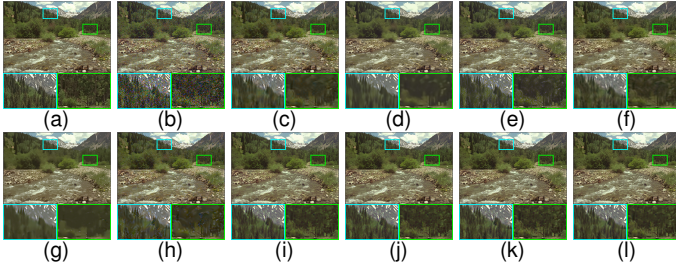


Fig. 7. Denoised results on “kodim13” ($[\sigma_{r,0}; \sigma_{g,0}; \sigma_{b,0}] = [30; 10; 50]$). (a) Ground truth. (b) Noisy observation (17.46, 0.5251). (c) CBM3D (25.45, 0.7100). (d) DRUNet (25.51, 0.6984). (e) Restormer (23.58, 0.6942). (f) HLTA-GN (25.05, 0.7228). (g) NGMeet (24.68, 0.6427). (h) DLRQP (25.38, 0.7233). (i) MCWNNM (27.07, 0.8094). (j) MCWSNM (27.25, 0.8049). (k) NNFNM (27.19, 0.8152). (l) DtNFM (**27.88 0.8360**).

channel $c \in \{r, g, b\}$ is given by

$$\sigma_c = \frac{\sigma_{c,0}}{512^2} \sum_{j=1}^{512} \sum_{i=1}^{512} \mathcal{M}(x, y). \quad (47)$$

The ground truth images are still taken from Kodak24 data set. And they are cropped to 512×512 pixels in order to match the size of the map \mathcal{M} . The upper-bounds of noise standard deviation $[\sigma_{r,0}; \sigma_{g,0}; \sigma_{b,0}] = [30; 35; 40]$. Considering the noise distribution, i.e., the map \mathcal{M} , is hard to estimate, we make all the competing methods be unaware of it. Consequently, they have to assume that the noise is spatially invariant. Thus

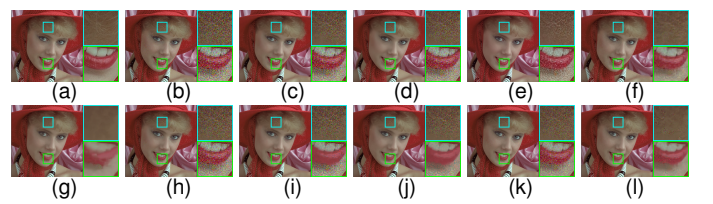


Fig. 9. Denoised results of “kodim04” (spatially variant noise). (a) Ground Truth. (b) Noisy observation (29.65, 0.8297). (c) CBM3D (32.70, 0.8712). (d) DRUNet (32.64, 0.8616). (e) Restormer (34.00, 0.8951). (f) HLTA-GN (34.54, 0.8867). (g) NGMeet (35.58, 0.9097). (h) DLRQP (33.15, 0.8838). (i) MCWNNM (33.09, 0.8697). (j) MCWSNM (33.41, 0.8534). (k) NNFNM (33.04, 0.8654). (l) DtNFM (**36.86, 0.9177**).

their flexibility on handling the noise can be fully tested. The parameters of DtNFM method are listed in Table V(c).

The PSNR and SSIM results are listed in Table VI. The proposed DtNFM achieves the highest PSNR on 20 images, and the highest SSIM on 16 images. And the average improvements of DtNFM over other methods are listed in Table IV(c). It demonstrates the DtNFM model has more flexibility in dealing with the spatially variant noise. In contrast, the MCWNNM, MCWSNM and NNFNM achieve sub-optimal performance since they are inadequate to handle the noise difference between the patches in the patch group.

The visual comparisons are shown in Fig. 9 and Fig. 10. The proposed DtNFM not only removes the noise more completely,

TABLE VI
PSNR AND SSIM RESULTS FOR ALL COMPETING METHODS IN THE SPATIALLY VARIANT NOISE EXPERIMENTS. RUNNING TIMES IS IN SECONDS.

#	CBM3D PSNR SSIM	DRUNet PSNR SSIM	Restormer PSNR SSIM	HLTA-GN PSNR SSIM	NGMeet PSNR SSIM	DLRQP PSNR SSIM	MCWNNM PSNR SSIM	MCWSNM PSNR SSIM	NNFNM PSNR SSIM	DtNFM PSNR SSIM
1	31.73 0.9231	31.79 0.9180	31.07 0.9231	30.46 0.8835	31.82 0.9121	32.00 0.9322	31.59 0.9205	29.41 0.8374	32.25 0.9277	33.91 0.9421
2	32.39 0.8583	32.84 0.8557	34.10 0.8917	32.17 0.8506	34.01 0.8835	32.81 0.8800	34.87 0.8849	32.59 0.8364	33.43 0.8775	35.65 0.9081
3	33.95 0.9175	33.85 0.9059	36.19 0.9207	35.54 0.9151	38.01 0.9438	33.63 0.8962	34.97 0.9186	35.44 0.9181	33.02 0.8749	38.58 0.9464
4	32.70 0.8712	32.64 0.8616	34.00 0.8951	34.54 0.8867	35.58 0.9097	33.15 0.8838	33.09 0.8697	33.41 0.8534	33.04 0.8654	36.86 0.9177
5	32.14 0.9485	32.54 0.9465	33.82 0.9582	28.62 0.8948	33.18 0.9529	31.75 0.9473	32.58 0.9464	30.94 0.9116	32.09 0.9473	33.87 0.9602
6	32.39 0.9017	32.50 0.8961	33.86 0.9291	32.56 0.9054	33.53 0.9159	32.49 0.9088	33.98 0.9196	31.32 0.8557	32.48 0.9059	34.65 0.9264
7	33.62 0.9352	33.59 0.9317	36.65 0.9517	33.81 0.9368	37.64 0.9620	33.40 0.9214	33.87 0.9273	34.63 0.9362	32.97 0.9125	37.77 0.9602
8	32.25 0.9295	32.21 0.9238	32.95 0.9376	31.00 0.9289	34.03 0.9446	31.75 0.9311	32.78 0.9355	31.35 0.9129	32.12 0.9277	34.19 0.9496
9	33.39 0.9098	33.50 0.9068	36.14 0.9215	35.03 0.9245	35.96 0.9265	33.24 0.8962	34.55 0.9105	34.62 0.9137	32.82 0.8770	37.03 0.9294
10	33.42 0.9013	33.33 0.8971	35.66 0.9122	34.83 0.9179	36.58 0.9255	33.22 0.8866	32.78 0.8856	34.44 0.8999	32.22 0.8604	36.95 0.9249
11	32.14 0.8993	32.24 0.8914	34.11 0.9226	31.44 0.8877	32.76 0.8986	32.32 0.9135	31.39 0.8932	31.51 0.8574	32.09 0.9040	34.22 0.9285
12	33.12 0.8846	32.88 0.8750	34.44 0.8999	35.76 0.9140	36.56 0.9156	33.13 0.8877	31.79 0.8682	33.72 0.8645	33.16 0.8742	36.98 0.9246
13	31.25 0.9263	31.40 0.9246	31.76 0.9346	28.48 0.8706	30.20 0.8568	30.99 0.9389	30.95 0.9353	28.63 0.8141	31.29 0.9423	31.53 0.9449
14	31.98 0.9018	32.22 0.8963	33.95 0.9308	29.91 0.8727	32.66 0.9078	32.15 0.9118	32.48 0.9065	30.59 0.8389	32.01 0.9082	33.87 0.9258
15	32.45 0.8743	32.91 0.8704	34.20 0.8955	32.18 0.8601	33.69 0.8904	32.82 0.8894	33.86 0.8851	32.66 0.8504	32.71 0.8747	35.66 0.9109
16	32.99 0.8971	32.73 0.8854	35.19 0.9223	34.25 0.8978	35.65 0.9157	33.05 0.8944	33.92 0.8888	32.55 0.8564	32.34 0.8755	36.57 0.9303
17	32.72 0.9005	32.80 0.8945	34.63 0.9214	31.89 0.8944	35.16 0.9194	32.73 0.9068	32.03 0.8870	32.95 0.8794	32.62 0.8900	34.71 0.9253
18	32.10 0.8949	32.20 0.8901	33.74 0.9215	28.14 0.8185	33.39 0.9125	32.21 0.8977	32.83 0.9047	30.72 0.8403	32.53 0.8928	33.93 0.9204
19	32.50 0.9263	32.78 0.9203	34.57 0.9314	33.83 0.9295	34.40 0.9273	32.68 0.9306	33.44 0.9208	32.67 0.9023	32.43 0.9177	35.77 0.9436
20	33.33 0.9074	34.21 0.9211	29.94 0.9086	35.33 0.9266	36.25 0.9464	33.26 0.8982	36.21 0.9413	33.51 0.8898	32.77 0.8865	35.76 0.9374
21	32.50 0.9134	32.60 0.9080	34.24 0.9333	32.36 0.9134	33.71 0.9243	32.45 0.9090	32.29 0.9021	31.68 0.8902	31.81 0.8903	34.60 0.9309
22	32.23 0.8826	32.38 0.8790	33.28 0.9010	33.01 0.8934	32.78 0.8864	32.49 0.8942	32.81 0.8854	31.68 0.8402	32.76 0.8853	34.97 0.9182
23	33.62 0.9006	33.34 0.8902	35.45 0.9139	35.74 0.9223	37.78 0.9434	33.34 0.8847	33.18 0.8811	35.08 0.9063	32.75 0.8657	37.95 0.9365
24	32.34 0.9200	32.63 0.9173	33.02 0.9291	31.21 0.9089	33.99 0.9234	32.48 0.9194	32.42 0.9170	31.98 0.8896	32.48 0.9078	34.78 0.9391
Avg.	32.64 0.9052	32.75 0.9003	34.04 0.9211	32.59 0.8981	34.56 0.9185	32.65 0.9067	33.11 0.9056	32.42 0.8748	32.51 0.8955	35.45 0.9326
Time	3.71	1.73	1.02	114.30	225.54	414.44	845.19	254.30	509.85	834.60

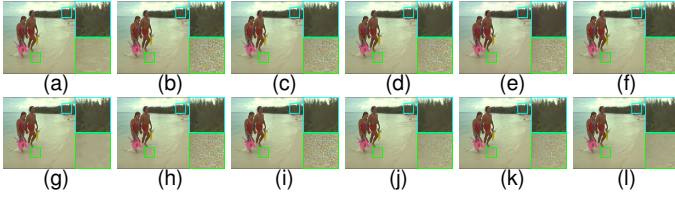


Fig. 10. Denoised results of “kodim12” (spatially variant noise). (a) Ground Truth. (b) Noisy observation (29.65, 0.8373). (c) CBM3D (33.12, 0.8846). (d) DRUNet (32.88, 0.8750). (e) Restormer (34.44, 0.8999). (f) HLTA-GN (35.76, 0.9140). (g) NGMeet (36.56, 0.9156). (h) DLRQP (33.13, 0.8877). (i) MCWNNM (31.79, 0.8682). (j) MCWSNM (33.72, 0.8645). (k) NNFNM (33.16, 0.8742). (l) DtNFM (**36.98, 0.9246**).

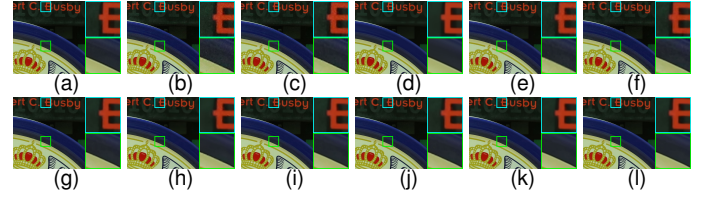


Fig. 11. Denoised results of image “#1” (real-world noise). (a) Ground Truth. (b) Noisy observation (37.00, 0.9345). (c) CBM3D (38.75, 0.9688). (d) DRUNet (40.88, 0.9805). (e) Restormer (36.88, 0.9718). (f) HLTA-GN (38.80, 0.9705). (g) NGMeet (41.14, 0.9830). (h) DLRQP (40.15, 0.9804). (i) MCWNNM (41.20, 0.9829). (j) MCWSNM (41.22, 0.9832). (k) NNFNM (41.24, 0.9835). (l) DtNFM (**41.43, 0.9837**).

and preserves more details, such as the hair and mouth in Fig. 9 and the trees at the top-right corner of Fig. 10. In contrast, the NGMeet over-smooth the images. Although the HLTA-GN removes the noise well, it is inadequate to preserve the textures. And the other seven methods remain too much noise. In summary, the proposed DtNFM method achieves a more rational balance between noise removal and detail protection.

C. Real-World Noise Removal

The real-world noise removal experiments are carried out on the CC15 dataset [54], which is shown in Fig. 5(b). It has 15 real-world noisy images and their noise-free versions. Those noise-free images are obtained by averaging each pixel from 500 images shot on the same scene under same camera settings. In practice, they can be used as the ground truth. With them, the PSNR and SSIM can be calculated for the quantitative comparison. For each corrupted image, the noise standard deviations $[\sigma_{r_0}; \sigma_{g_0}; \sigma_{b_0}]$ are estimated by a state-of-the-art noise estimation method [51]. Then, the competing methods denoise the images under the assumption that the

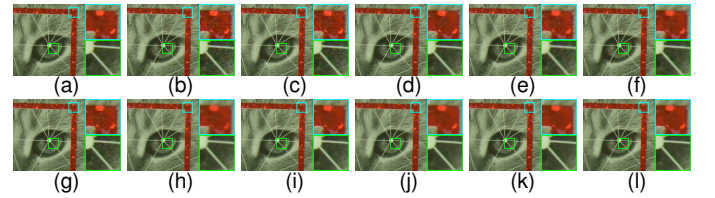


Fig. 12. Denoised results of image “#15” (real-world noise). (a) Ground Truth. (b) Noisy observation (29.87, 0.7835). (c) CBM3D (30.48, 0.8146). (d) DRUNet (33.83, 0.9215). (e) Restormer (32.15, 0.8839). (f) HLTA-GN (33.66, 0.9181). (g) NGMeet (33.18, 0.9037). (h) DLRQP (33.30, 0.9091). (i) MCWNNM (33.97, 0.9215). (j) MCWSNM (33.78, 0.9167). (k) NNFNM (34.14, 0.9245). (l) DtNFM (**34.25, 0.9255**).

noise is spatially invariant. The parameters of DtNFM method are listed in Table V(d).

The PSNR and SSIM results are listed in Table VII. As can be seen, DtNFM achieves the highest PSNR and SSIM on 5 images. And it achieves the highest average PSNR and SSIM. The average PSNR and SSIM improvements of DtNFM over other methods are listed in Table IV(d). We also compare the DtNFM with other mainstream deep learning-based methods,

TABLE VII
PSNR AND SSIM RESULTS FOR ALL COMPETING METHODS IN THE REAL-WORLD NOISE EXPERIMENTS. RUNNING TIMES IS IN SECONDS.

#	CBM3D PSNR SSIM	DRUNet PSNR SSIM	Restormer PSNR SSIM	HLTA-GN PSNR SSIM	NGMeet PSNR SSIM	DLRQP PSNR SSIM	MCWNNM PSNR SSIM	MCWSNM PSNR SSIM	NNFNM PSNR SSIM	DtNFM PSNR SSIM
1	38.75 0.9688	40.88 0.9805	36.88 0.9718	38.80 0.9705	41.14 0.9830	40.15 0.9804	41.20 0.9829	41.22 0.9832	41.24 0.9835	41.43 0.9837
2	35.52 0.9407	36.83 0.9486	36.71 0.9545	36.49 0.9517	37.32 0.9593	37.04 0.9585	37.25 0.9587	37.34 0.9608	37.25 0.9607	37.27 0.9592
3	35.69 0.9583	36.00 0.9542	35.65 0.9644	36.38 0.9640	37.08 0.9691	36.66 0.9631	37.06 0.9694	36.99 0.9670	36.96 0.9683	36.98 0.9665
4	33.84 0.9220	35.50 0.9603	34.41 0.9545	34.81 0.9466	34.59 0.9463	34.89 0.9470	35.54 0.9598	35.28 0.9559	35.54 0.9600	35.49 0.9591
5	34.66 0.9050	37.15 0.9602	36.10 0.9560	36.07 0.9436	36.58 0.9490	36.22 0.9468	37.03 0.9568	36.66 0.9524	37.10 0.9584	37.18 0.9590
6	36.22 0.9062	40.44 0.9810	38.09 0.9686	39.55 0.9735	40.29 0.9795	39.03 0.9692	39.56 0.9711	39.53 0.9710	41.27 0.9874	41.18 0.9873
7	36.63 0.9297	39.69 0.9705	38.70 0.9630	37.94 0.9546	38.77 0.9654	38.46 0.9605	39.26 0.9674	39.07 0.9668	39.35 0.9687	39.30 0.9676
8	37.32 0.9296	42.31 0.9832	38.93 0.9683	39.84 0.9730	40.86 0.9767	39.53 0.9655	41.45 0.9782	41.15 0.9768	41.84 0.9816	42.07 0.9822
9	36.31 0.9006	39.97 0.9580	39.31 0.9481	37.96 0.9417	39.05 0.9532	38.60 0.9488	39.54 0.9561	39.39 0.9564	39.70 0.9556	39.65 0.9585
10	34.40 0.8647	39.30 0.9683	37.83 0.9434	38.78 0.9616	38.32 0.9639	38.48 0.9614	38.94 0.9636	38.89 0.9633	39.66 0.9749	39.71 0.9736
11	33.54 0.8743	36.73 0.9486	37.82 0.9584	37.22 0.9535	36.52 0.9426	36.47 0.9444	37.40 0.9524	37.23 0.9517	37.84 0.9586	37.65 0.9561
12	34.24 0.8352	41.10 0.9775	37.40 0.9177	39.93 0.9682	38.65 0.9572	39.45 0.9589	39.42 0.9591	39.52 0.9599	42.77 0.9832	42.99 0.9845
13	30.64 0.7691	35.65 0.9398	31.94 0.8294	33.33 0.9097	35.50 0.9305	32.88 0.8841	34.85 0.9221	34.47 0.9200	35.18 0.9371	35.52 0.9381
14	30.88 0.8473	34.24 0.9486	32.70 0.9208	33.12 0.9257	34.00 0.9392	32.51 0.9045	33.97 0.9397	33.56 0.9336	34.06 0.9471	34.20 0.9490
15	30.48 0.8146	33.83 0.9215	32.15 0.8839	33.66 0.9181	33.18 0.9037	33.30 0.9091	33.97 0.9215	33.78 0.9167	34.14 0.9245	34.25 0.9255
Avg.	34.61 0.8911	37.98 0.9601	36.31 0.9402	36.93 0.9504	37.46 0.9546	36.91 0.9468	37.76 0.9572	37.6 0.9557	38.26 0.9633	38.32 0.9633
Time	4.34	0.78	1.39	724.03	106.36	589.8	295.3	294.3	317.06	325.95

TABLE VIII
ABLATION EXPERIMENTS FOR THE DtNFM MODEL.

Model	Noise	
	Spatially invariant Std = [30; 10; 50]	Spatially variant Std = [30; 35; 40]
	PSNR SSIM	PSNR SSIM
(a) DtNFM	31.94 0.8720	35.45 0.9326
(b) DtNFM-C	27.53 0.7042	32.78 0.9079
(c) DtNFM-S	31.87 0.8701	35.27 0.9313

including the Uformer [55], DeamNet [13], DudeNet [56], SADNet [57], and FFDNet [10]. Due to space limit, the PSNR and SSIM results are shown in the supplementary material.

The visual comparisons are shown in Fig. 11 and Fig. 12. The DtNFM generates satisfactory visual quality, removing the noise fully and preserves image details well. In contrast, CBM3D and Restormer remain some noise, and the DLRQP over-smooth the images. To sum up, the proposed DtNFM has strong capacity on reducing the real-world noise, achieving higher PSNR and SSIM and producing promising visual quality.

D. Ablation Studies

In the proposed DtNFM model (14), the weight matrices \mathbf{C} and \mathbf{S} are used at once. To find their contributions, the ablation experiments are carried out. For the DtNFM model (baseline), the following two models can be generated by it:

$$\arg \min_{\mathbf{X} \in \mathbb{R}^{3d^2 \times N}} \|(\mathbf{Y} - \mathbf{X})\mathbf{S}\|_F^2 + \lambda \|\mathbf{X}\|_{t,*-F}, \quad (48)$$

$$\arg \min_{\mathbf{X} \in \mathbb{R}^{3d^2 \times N}} \|\mathbf{C}(\mathbf{Y} - \mathbf{X})\|_F^2 + \lambda \|\mathbf{X}\|_{t,*-F}, \quad (49)$$

where $\mathbf{S} = \text{Diag}([\sigma_1^{-1}, \dots, \sigma_N^{-1}]) \in \mathbb{R}^{N \times N}$, $\mathbf{C} = \text{Diag}([\sigma_r^{-1} \mathbf{1}; \sigma_g^{-1} \mathbf{1}; \sigma_b^{-1} \mathbf{1}]) \in \mathbb{R}^{3d^2 \times 3d^2}$, $\mathbf{1} \in \mathbb{R}^{d^2}$ is a column vector of ones, and the definition of σ_c ($c \in \{r, g, b\}$), σ_j ($j \in \{1, \dots, N\}$) can be found in Section III.A. And the models in (48) and (49) are respectively denoted as “DtNFM-C” and “DtNFM-S”. Two kinds of noise are tested, as shown in the last two columns of Table VIII.

The results of the ablation experiments are reported in Table VIII. Note that the PSNR and SSIM are averaged by the 24

images in Kodak24 dataset. And the parameters are all kept the same. We have the following observations:

- Table VIII(b) demonstrates the weight matrix \mathbf{C} provides a gain of (4.41dB, 0.1678) in the spatially invariant noise removal. And its gain reduces to (2.67dB, 0.0247) in the spatially variant noise removal. Hence the matrix \mathbf{C} would provide more contribution when removing the spatially invariant noise.
- Table VIII(c) demonstrates the weight matrix \mathbf{S} provides a gain of (0.07dB, 0.0019) in the spatially invariant noise removal. And its contribution improves to (0.18dB, 0.0013) in the spatially variant noise removal. Hence the matrix \mathbf{S} would provide more contribution when removing the spatially variant noise.

However, one may point out that the contribution of matrix \mathbf{S} is significantly smaller than that of matrix \mathbf{C} in both two experiments. We believe this will be alleviated if a more reasonable scheme is used to determine the relative weight $p \in [0, 1]$ between \mathbf{C} and \mathbf{S} .

E. The Impact of the Hyper-parameters λ and t

To give empirical schemes for determining the hyper-parameters λ and t , we analysis their impacts on the model performance. All the test images are taken from Kodak24 data set. The corrupted images are generated by the spatially invariant noise with $[\sigma_{r_0}; \sigma_{g_0}; \sigma_{b_0}] = [30; 10; 50]$. All the parameters are fixed but λ and t .

The regularization parameter λ is the most important parameter. It controls the regularization effects of the objective function in (14), and further controls the trade-off between noise removal and details preserving. Concretely, as it becomes too small, a resultant DtNFM model will suffer from overfitting since it mostly minimize the loss term in (14). Consequently, the output image will contain too much noise, as shown in Fig. 13(a), Fig. 13(d), and Fig. 13(g). On the contrary, as λ becomes too large, a resultant DtNFM model may suffer from underfitting since it minimizes the regularization term too much. Consequently, the output image may be over-smoothed, losing too many details, such as the Fig. 13(c). However, the problem of over-smoothing will be alleviated as t becomes

TABLE IX
GROUPING RESULTS OF THE 24 TEST IMAGES.

Group 1	Image#	23	3	12	20	2	15	9	10	Avg(t)	Std(t)
	$SSIM_0$	0.2523	0.2578	0.2687	0.2754	0.2763	0.2785	0.2885	0.2930		
	Best t	2	2	3	3	3	4	3	5		
Group 2	Image#	4	17	16	7	22	11	21	19	Avg(t)	Std(t)
	$SSIM_0$	0.2962	0.3060	0.3123	0.3320	0.3390	0.3541	0.3592	0.3636		
	Best t	3	3	4	3	5	6	6	5		
Group 3	Image#	6	18	24	14	1	5	13	8	Avg(t)	Std(t)
	$SSIM_0$	0.3895	0.3967	0.3989	0.4037	0.4783	0.4888	0.5251	0.5418		
	Best t	5	7	8	7	7	7	10	3		

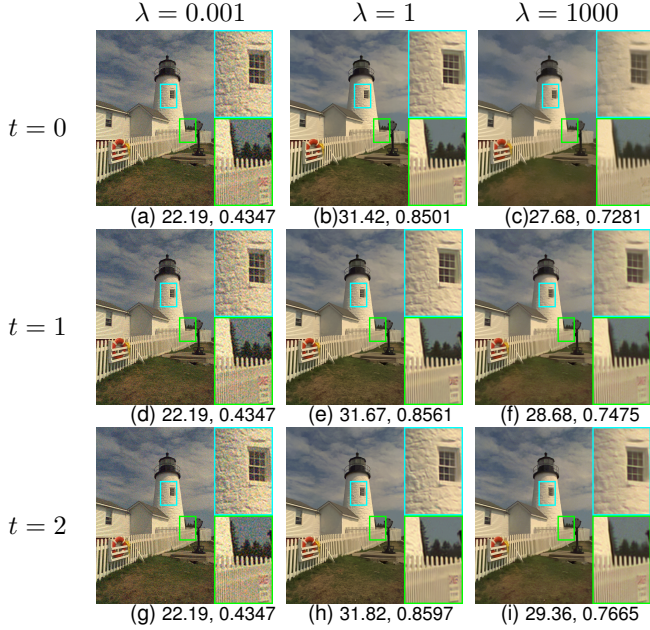


Fig. 13. Denoised results of “kodim19” with different values of λ and t .

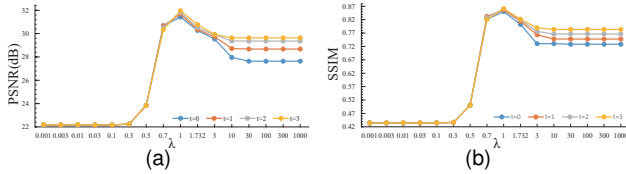


Fig. 14. PSNR and SSIM results of “kodim19” on the grid of λ and t .

larger, as shown in Fig. 13(f) and Fig. 13(i). That is because the t most dominant rank components of the observed patch matrix \mathbf{Y} are preserved without any condition. Therefore, the more information can be preserved.

Although a larger t can protect the image from over-smoothing, the resultant DtNFM model is still inadequate to be performant. As shown in Fig. 14, suboptimal PSNR and SSIM will be obtained when λ is too large for all t . While the optimal values of λ dwell around 1.0. Therefore, determining the λ needs at least a line search.

The parameter $t \in \mathbb{N}$ also impacts the model performance, since it controls the shrinkage on the singular values. Fig. 15 shows the shrinkage performed by the tNF regularizer, i.e., the proximal operator (33). We can see that as t becomes

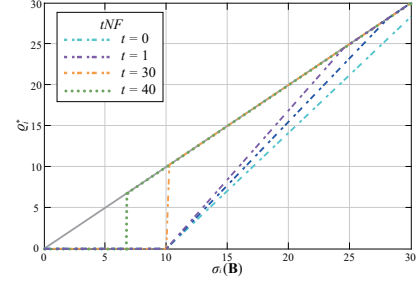


Fig. 15. The shrinkage functions of the proximal operator (33) with $\tau = 10$.

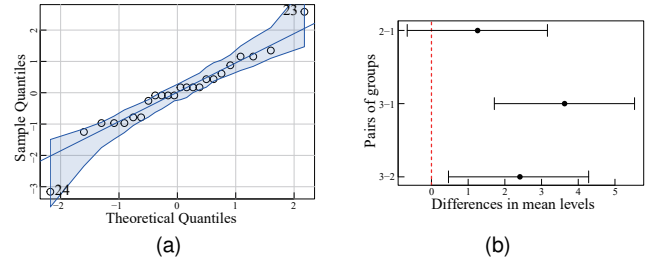


Fig. 16. (a) Test the normality via the Q-Q plot. (b) Multiple comparisons between all pairs.

too small, the leading singular values may not be preserved well. Hence the model may over-smooth the image, as is the case in Fig. 13(c). On the contrary, as t becomes larger, more singular values would be preserved. Hence more noise would be preserved, since the inputted singular values come from the SVD of the corrupted data matrix. Therefore, the choice of t should be judicious.

We give an empirical scheme in which a better t can be determined by analyzing the SSIM of the corrupted image, denoted as $SSIM_0$. Given a corrupted image, the higher its $SSIM_0$ is, a larger t is preferred. This is verified by the analysis of variance (ANOVA). Concretely, we first sort the $SSIM_0$ of 24 corrupted images in an ascending order. Based on the order, the 24 corrupted images are broke up into 3 groups, as shown in Table IX. Then, we search the best t for each image, and list them in Table IX. As shown in the rightmost column, the average of “Best t ” of Group 1 is the smallest, while that of Group 3 is the largest. This intuitive observation implies an connection between the $SSIM_0$ and the “Best t ”. Now we resort to the ANOVA to prove there exist a significant difference between the averages of “Best t ”.

To perform the ANOVA, the dependent variable t should be

TABLE X
THE TABLE OF ANOVA.

Source	Sum of Squares	Degrees of Freedom	Mean Square	F	p
Inter-group	67.13	2	33.56	20.86	1.28×10^{-5}
Within-group	32.18	20	1.61		
Total	99.30	22			

normally distributed and have an equal variance in each group. The normality assumption can be assessed via the Q-Q plot, shown in Fig. 16a. As can be seen, the normality assumption is satisfied since all of the points fall within the 95% confidence envelope, and the slope of the main diagonal is closed to 1.0. The equality of variances can be checked via the Barlett's test. And the result ($p = 0.165$) suggests that the variances in three groups do not differ significantly. Hence the ANOVA can be carried out.

The results of ANOVA are shown in Table X. As $p < 0.05$, the average of “best t ” does have a significant difference among three groups. Although the multiple comparisons in Fig. 16b demonstrate that the averages of “best t ” in group 1 and 2 are not significantly different, it is still easy to find the positive correlation between $SSIM_0$ and “best t ”.

V. CONCLUSION

In this paper, the DtNFM model was proposed and applied to color image denoising via integrating with the NSS prior. The DtNFM model possesses two advantages. On the one hand, it can fully model and utilize the cross-channel difference and the spatial variation of noise. On the other hand, it can provide flexible treatments for different rank components, and further give a close approximation to the underlying low-rank matrix. To solve the resultant optimization problem, an accurate and effective algorithm was proposed by exploiting the framework of ADMM. Importantly, we mathematically proved the global optima of all subproblems can be obtained in closed-form. The convergence guarantee was established. Extensive experiments are carried out on the synthetic noise, spatially variant noise, and real-world noise images, respectively. The results demonstrated that the proposed method outperforms many state-of-the-art color image denoising methods.

In the future, we will try to extend our work to low-rank tensor approximation. If so, we would no longer have to stretch the similar patches to vectors. Hence the structure of patches would be preserved better. Moreover, we will try to devise heuristic schemes to search and update the t and α adaptively. If so, the practicality of the proposed DtNFM model would be further improved.

REFERENCES

- [1] S. Minaee, Y. Boykov, F. Porikli, A. Plaza, N. Kehtarnavaz, and D. Terzopoulos, “Image segmentation using deep learning: A survey,” *IEEE Trans. Pattern Anal. and Mach. Intell.*, vol. 44, no. 7, pp. 3523–3542, Jul. 2022.
- [2] H. Sheng, R. Cong, D. Yang, R. Chen, S. Wang, and Z. Cui, “Urbanlf: A comprehensive light field dataset for semantic segmentation of urban scenes,” *IEEE Trans. Circuits Syst. Video Technol.*, vol. 32, no. 11, pp. 7880–7893, Nov. 2022.
- [3] X. Wang, D. Peng, M. Yan, and P. Hu, “Correspondence-free domain alignment for unsupervised cross-domain image retrieval,” in *Proc. AAAI Conf. Artif. Intell.*, 2023, pp. 10 200–10 208.
- [4] X. Wang, D. Peng, P. Hu, Y. Gong, and Y. Chen, “Cross-domain alignment for zero-shot sketch-based image retrieval,” *IEEE Trans. Circuits Syst. Video Technol.*, vol. 33, no. 11, pp. 7024–7035, Nov. 2023.
- [5] D.-Y. Chen, C.-C. Chen, and L.-W. Kang, “Visual depth guided color image rain streaks removal using sparse coding,” *IEEE Trans. Circuits Syst. Video Technol.*, vol. 24, no. 8, pp. 1430–1455, Aug. 2014.
- [6] L. Liu, C. L. P. Chen, X. You, Y. Y. Tang, Y. Zhang, and S. Li, “Mixed noise removal via robust constrained sparse representation,” *IEEE Trans. Circuits Syst. Video Technol.*, vol. 28, no. 9, pp. 2177–2189, Sep. 2018.
- [7] L. Sha, D. Schonfeld, and J. Wang, “Graph laplacian regularization with sparse coding for image restoration and representation,” *IEEE Trans. Circuits Syst. Video Technol.*, vol. 30, no. 7, pp. 2000–2014, Jul. 2020.
- [8] H. Liu, J. Zhang, and R. Xiong, “Cas: Correlation adaptive sparse modeling for image denoising,” *IEEE Trans. Comput. Imag.*, vol. 7, pp. 638–647, May 2021.
- [9] B. Jiang, Y. Lu, B. Zhang, and G. Lu, “Few-shot learning for image denoising,” *IEEE Trans. Circuits Syst. Video Technol.*, vol. 33, no. 9, pp. 4741–4753, Sep. 2023.
- [10] K. Zhang, W. Zuo, and L. Zhang, “FFDNet: Toward a fast and flexible solution for cnn-based image denoising,” *IEEE Trans. Image Process.*, vol. 27, no. 9, pp. 4608–4622, Sep. 2018.
- [11] K. Zhang, W. Zuo, Y. Chen, D. Meng, and L. Zhang, “Beyond a gaussian denoiser: Residual learning of deep cnn for image denoising,” *IEEE Trans. Image Process.*, vol. 26, no. 7, pp. 3142–3155, Jul. 2017.
- [12] K. Zhang, Y. Li, W. Zuo, L. Zhang, L. Van Gool, and R. Timofte, “Plug-and-play image restoration with deep denoiser prior,” *IEEE Trans. Pattern Anal. Mach. Intell.*, vol. 44, no. 10, pp. 6360–6376, Oct. 2021.
- [13] C. Ren, X. He, C. Wang, and Z. Zhao, “Adaptive consistency prior based deep network for image denoising,” in *Proc. IEEE Conf. Comput. Vis. Pattern Recognit.*, June 2021, pp. 8596–8606.
- [14] W. Xu, Q. Zhu, N. Qi, and D. Chen, “Deep sparse representation based image restoration with denoising prior,” *IEEE Trans. Circuits Syst. Video Technol.*, vol. 32, no. 10, pp. 6530–6542, Apr. 2022.
- [15] X. Zhang, J. Zheng, D. Wang, and L. Zhao, “Exemplar-based denoising: A unified low-rank recovery framework,” *IEEE Trans. Circuits Syst. Video Technol.*, vol. 30, pp. 2538–2549, Aug. 2020.
- [16] T. Xu, X. Kong, Q. Shen, Y. Chen, and Y. Zhou, “Deep and low-rank quaternion priors for color image processing,” *IEEE Trans. Circuits Syst. Video Technol.*, vol. 33, no. 7, pp. 3119–3132, Jul. 2023.
- [17] H. Wang, Y. Li, Y. Cen, and Z. He, “Multi-matrices low-rank decomposition with structural smoothness for image denoising,” *IEEE Trans. Circuits Syst. Video Technol.*, vol. 30, no. 2, pp. 349–361, Feb. 2020.
- [18] M. Xie, X. Liu, and X. Yang, “Novel hybrid low-rank tensor approximation for hyperspectral image mixed denoising based on global-guided-nonlocal prior mechanism,” *IEEE Trans. Geosci. Remote Sens.*, vol. 60, pp. 1–17, Oct. 2022.
- [19] J. Xu, L. Zhang, D. Zhang, and X. Feng, “Multi-channel weighted nuclear norm minimization for real color image denoising,” in *Proc. IEEE Int. Conf. Comput. Vis.*, 2017, pp. 1105–1113.
- [20] X. Huang, B. Du, and W. Liu, “Multichannel color image denoising via weighted Schatten p -norm minimization,” in *Proc. Int. Joint Conf. Artif. Intell.*, 2020, pp. 637–644.
- [21] Y. Shan, D. Hu, Z. Wang, and T. Jia, “Multi-channel nuclear norm minus Frobenius norm minimization for color image denoising,” *Signal Process.*, vol. 207, p. 108959, Jun. 2023.
- [22] A. Buades, B. Coll, and J.-M. Morel, “A non-local algorithm for image denoising,” in *Proc. IEEE Conf. Comput. Vis. Pattern Recognit.*, 2005, pp. 60–65.
- [23] S. Wang, L. Zhang, and Y. Liang, “Nonlocal spectral prior model for low-level vision,” in *Proc. Asi. Conf. Comput. Vis.*, 2012, p. 231–244.
- [24] E.-J. Candès and B. Recht, “Exact matrix completion via convex optimization,” *Found. Comput. Math.*, vol. 9, no. 6, pp. 717–772, Apr. 2009.
- [25] D. Donoho, “Compressed sensing,” *IEEE Trans. Inf. Theory*, vol. 52, no. 4, pp. 1289–1306, Apr. 2006.
- [26] M. Fazel, H. Hindi, and S. Boyd, “A rank minimization heuristic with application to minimum order system approximation,” in *Proc. American Control Conf.*, 2001, pp. 4734–4739.
- [27] J. Cai, E.-J. Candès, and Z. Shen, “A singular value thresholding algorithm for matrix completion,” *SIAM J. Optim.*, vol. 20, no. 4, pp. 1956–1982, Mar. 2010.
- [28] S. Ma, D. Goldfarb, and L. Chen, “Fixed point and bregman iterative methods for matrix rank minimization,” *Mathematical Programming*, vol. 128, pp. 321–353, Sep. 2011.

- [29] K. Toh and S. Yun, "An accelerated proximal gradient algorithm for nuclear norm regularized linear least squares problems," *Pac. J. Optim.*, vol. 6, no. 615-640, p. 15, Mar. 2010.
- [30] S. Gu, Q. Xie, D. Meng, W. Zuo, X. Feng, and L. Zhang, "Weighted nuclear norm minimization and its applications to low level vision," *Int. J. Comput. Vis.*, vol. 121, p. 183-208, Jul. 2017.
- [31] S. Gu, L. Zhang, W. Zuo, and X. Feng, "Weighted nuclear norm minimization with application to image denoising," in *Proc. IEEE Int. Conf. Comput. Vis.*, 2014, pp. 2862-2869.
- [32] Y. Chen, X. Xiao, and Y. Zhou, "Low-rank quaternion approximation for color image processing," *IEEE Trans. Image Process.*, vol. 29, pp. 1426-1439, Sep. 2020.
- [33] T.-H. Oh, Y.-W. Tai, J.-C. Bazin, H. Kim, and I. Kweon, "Partial sum minimization of singular values in robust pca: Algorithm and applications," *IEEE Trans. Pattern Anal. Mach. Intell.*, vol. 38, no. 4, pp. 744-758, Apr. 2016.
- [34] Y. Wang, Q. Yao, and J. Kwok, "A scalable, adaptive and sound nonconvex regularizer for low-rank matrix learning," in *Proc. Int. World Wide Web Conf.*, 2021, p. 1798-1808.
- [35] Z. Wang, Y. Liu, X. Luo, J. Wang, C. Gao, D. Peng, and W. Chen, "Large-scale affine matrix rank minimization with a novel nonconvex regularizer," *IEEE Trans. Neural Netw. Learn. Syst.*, vol. 33, no. 9, pp. 4661-4675, Sep. 2022.
- [36] Z. Wang, W. Wang, J. Wang, and S. Chen, "Fast and efficient algorithm for matrix completion via closed-form 2/3-thresholding operator," *Neurocomputing*, vol. 330, pp. 212-222, Feb. 2019.
- [37] Z. Wang, D. Hu, X. Luo, W. Wang, J. Wang, and W. Chen, "Performance guarantees of transformed Schatten-1 regularization for exact low-rank matrix recovery," *Int. J. Mach. Learn. Cybern.*, vol. 12, pp. 3379-3395, Jun. 2021.
- [38] Z. Wang, C. Gao, X. Luo, M. Tang, J. Wang, and W. Chen, "Accelerated inexact matrix completion algorithm via closed-form q -thresholding ($q = 1/2, 2/3$) operator," *Int. J. Mach. Learn. Cybern.*, vol. 11, pp. 2327-2339, Apr. 2020.
- [39] Y. Xie, S. Gu, Y. Liu, W. Zuo, W. Zhang, and L. Zhang, "Weighted Schatten p -norm minimization for image denoising and background subtraction," *IEEE Trans. Image Process.*, vol. 25, no. 10, pp. 4842-4857, Oct. 2016.
- [40] W. Zuo, D. Meng, L. Zhang, X. Feng, and D. Zhang, "A generalized iterated shrinkage algorithm for non-convex sparse coding," in *Proc. IEEE Int. Conf. Comput. Vis.*, 2013, pp. 217-224.
- [41] K. Dabov, A. Foi, V. Katkovnik, and K. Egiazarian, "Color image denoising via sparse 3d collaborative filtering with grouping constraint in luminance-chrominance space," in *Proc. IEEE Int. Conf. Image Process.*, vol. 1, 2007, pp. I - 313-I - 316.
- [42] Y. Yu, Y. Zhang, and S. Yuan, "Quaternion-based weighted nuclear norm minimization for color image denoising," *Neurocomputing*, vol. 332, pp. 283-297, Mar. 2019.
- [43] T. Ma, Y. Lou, and T. Huang, "Truncated ℓ_1 - ℓ_2 models for sparse recovery and rank minimization," *SIAM Journal on Imaging Sciences*, vol. 10, no. 3, pp. 1346-1380, Aug. 2017.
- [44] G. Liu, Z. Lin, S. Yan, J. Sun, Y. Yu, and Y. Ma, "Robust recovery of subspace structures by low-rank representation," *IEEE Trans. Pattern Anal. Mach. Intell.*, vol. 35, no. 1, pp. 171-184, Apr. 2013.
- [45] T. Liu, D. Hu, Z. Wang, J. Gou, and W. Chen, "Hyperspectral image denoising using nonconvex fraction function," *IEEE Geosci. Remote Sens. Lett.*, vol. 20, p. Article 5508105, 2023.
- [46] Z. Liu, D. Hu, Z. Wang, J. Gou, and T. Jia, "Latlr for subspace clustering via reweighted Frobenius norm minimization," *Expert Syst. Appl.*, vol. 224, p. 119977, Aug. 2023.
- [47] M. Xie, X. Liu, X. Yang, and W. Cai, "Multichannel image completion with mixture noise: Adaptive sparse low-rank tensor subspace meets nonlocal self-similarity," *IEEE Trans. Cybern.*, vol. 53, no. 12, pp. 7521-7534, May 2023.
- [48] M. Xie, X. Liu, and X. Yang, "A nonlocal self-similarity-based weighted tensor low-rank decomposition for multichannel image completion with mixture noise," *IEEE Trans. Neural Netw. Learn. Syst.*, vol. 35, no. 1, pp. 73-87, May 2022.
- [49] J.-B. Hiriart-Urruty, "Generalized differentiability / duality and optimization for problems dealing with differences of convex functions," in *Proc. Convexity and Duality in Optimization*, 1985, pp. 37-70.
- [50] B. Leung, G. Jeon, and E. Dubois, "Least-squares luma-chroma demultiplexing algorithm for Bayer demosaicking," *IEEE Trans. Image Process.*, vol. 20, no. 7, pp. 1885-1894, Jul. 2011.
- [51] G. Chen, F. Zhu, and P. Heng, "An efficient statistical method for image noise level estimation," in *Proc. IEEE Int. Conf. Comput. Vis.*, 2015, pp. 477-485.
- [52] S. W. Zamir, A. Arora, S. Khan, M. Hayat, F. S. Khan, and M. Yang, "Restormer: Efficient transformer for high-resolution image restoration," in *Proc. IEEE Conf. Comput. Vis. Pattern Recognit.*, 2022, pp. 5718-5729.
- [53] W. He, Q. Yao, C. Li, N. Yokoya, Q. Zhao, H. Zhang, and L. Zhang, "Non-local meets global: An iterative paradigm for hyperspectral image restoration," *IEEE Trans. Pattern Anal. and Mach. Intell.*, vol. 44, no. 4, pp. 2089-2107, 2022.
- [54] S. Nam, Y. Hwang, Y. Matsushita, and S. J. Kim, "A holistic approach to cross-channel image noise modeling and its application to image denoising," in *Proc. IEEE Int. Conf. Comput. Vis.*, 2016, pp. 1683-1691.
- [55] Z. Wang, X. Cun, J. Bao, W. Zhou, J. Liu, and H. Li, "Uformer: A general u-shaped transformer for image restoration," in *Proc. IEEE Int. Conf. Comput. Vis.*, 2022, pp. 17662-17672.
- [56] C. Tian, Y. Xu, W. Zuo, B. Du, C.-W. Lin, and D. Zhang, "Designing and training of a dual cnn for image denoising," *Knowl. Based Syst.*, vol. 226, p. 106949, Aug. 2021.
- [57] M. Chang, Q. Li, H. Feng, and Z. Xu, "Spatial-adaptive network for single image denoising," in *Eur. Conf. Comput. Vis.*, 2020, pp. 171-187.